2802

BERICHTE
aus dem
INSTITUT FÜR MEERESKUNDE
an der
CHRISTIAN–ALBRECHTS–UNIVERSITÄT · KIEL

Nr. 297

Study of Passive Remote Sensing of the Atmosphere and Surface Ice

DOI 10.2289/IFM-BER_297

Rolf Fuhrhop
Angewandte Meteorologie und Fernerkundung, Kiel

Clemens Simmer und Meeno Schrader
Institut für Meereskunde, Kiel

Georg Heygster und Klaus–Peter Johnsen
Institut für Umweltphysik, Universität Bremen

Peter Schlüssel
Meteorologisches Institut, Universität Hamburg

Institut für Meereskunde an der Universität Kiel

December 1996

Executive Summary and Final Report
ESA ESTEC Contract No. 11198/94/NL/CN
Scientific Study Leader : Josef Noll
Technical Officer : Mike Wintzer

EUROPEAN SPACE AGENCY CONTRACT REPORT
The work in this report was done under ESA contract. Responsibility for the contents resides in the author or organization that prepared it.

Copies of this report can be obtained from

Institute for Marine Sciences
Dept. of Marine Meteorology
Düsternbrooker Weg 20
D- 24105 Kiel
Germany

Abstract

A radiative transfer model to compute brightness temperatures in the microwave frequency range for polar regions including sea ice, open ocean and atmosphere has been developed. The calculation of the sea-ice reflectivity is incorporated by the 'many layer strong fluctuation theory' model of Grenfell and Stogryn. The surface reflectivity of the open water is computed with three scale model of Schrader. Both surface models supply the bistatic scattering coefficients, which define the lower boundary for the atmospheric model. The atmospheric model computes the gaseous absorption of water vapour and oxygen by the Liebe model. Cloud hydrometeors are considered by Mie- or Rayleigh- scattering.

The radiative transfer model has been validated for SSM/I frequencies using six test cases. The ground truth data (surface and atmosphere) has been observed during the ARKTIS'88 and ARKTIS'93 experiments. The simulated brightness temperatures are compared to collocated SSM/I measurements. The validation exhibits shortcomings of the sea-ice model for 37 GHz. The actual reasons for these deviations are unknown, but a possible explanation is an artificial oscillation of the reflectivity as function of frequency and ice-layer thickness. An empirical correction of the reflectivity for this frequncy has been derived and its application gives consistent comparison results between the simulated and observed brightness temperatures within the accuracy range.

The sensitivity study for the simulated brightness temperatures shows that the strongest influence originates from the sea-ice concentration, due to the large emissivity differences between open water and sea ice. Atmospheric clouds, wind speed over open water, and the snow layer overlaying the sea ice affect the simulated brightness temperatures significantly. These parameters have considerable effect on the polarization and gradient ratios. Therefore they influence a sea-ice retrieval algorithm when based on these ratios as for instance the NASA sea ice algorithm. Simulated brightness temperatures have been used to train a neural network algorithm for the total sea ice concentration, which accounts for these effects. Sea-ice concentrations sensed from SSM/I data using the neural network approach and the NASA sea-ice algorithm show systematic differences in dependency on cloudiness.

Executive Summary

Introduction

The understanding of passive microwave signatures from sea ice has been improved over the past two decades using sensors located at the surface, on aircrafts, and on satellites. Early studies, which used data obtained mainly from aircrafts and satellites, show that three dominant surface types (open water, first–year ice, multiyear ice) could be discriminated. These observations established the basis for the development of retrieval algorithms, which are currently used to sense sea ice concentrations from satellite observations.

The sea ice retrieval with passive microwave sensors on satellites has mostly regarded the atmospheric contributions as inevitable, but neglectable noise. Retrieval of atmospheric paramerters from satellites over the open ocean works satisfactorily due to the low emissivity of the surface, and the compensating effects of sea surface temperature and sea water emissivity, i.e. the emission is nearly independent from the sea surface temperature. The emission of the sea ice surface does not offer these advantages. The sea ice dominates the radiation signal, and the retrieval quality of atmospheric parameters is largely reduced. To improve the retrieval of sea ice and atmospheric parameters over the ice covered ocean, the integration of individual radiative transfer models for sea ice, open ocean, and atmosphere is required. The combined model will give the opportunity to study the radiative signatures of the individual components and of the total environment. The goal of this study is to combine radiative transfer models for the individual environments into one integrated model. Simulated brightness temperatures calculated from the model will be used to derive algorithms for the retrieval of geophysical parameters.

The Combined Model

The combined model is made up of three individual radiation models for the sea ice covered ocean, open ocean, and atmosphere. The output of the model are brightness temperatures, which include the effects of the individual components.

Sea Ice Module

There are essentially two widely disparate analytic approaches available to study the radiative signatures from sea ice; radiative transfer models with scattering and models based on the solution of Maxwell's equations with random perturbations in the dielectric properties. The radiative transfer approach has been by far the most popular one in the past, no

doubt due to its relative simplicity. Unfortunately, there are strong arguments against its applicability. The most important are: 1) The ice grains and snow crystals are so closely packed that the scatterers in the vicinity of a particular grain are in its near field. Thus, the application of far field scattering coefficients commonly used in radiative transfer models is inappropriate. 2) Coupling effects between particles are ignored. 3) Further, radiative transfer models have generally used Mie scattering theory to determine scattering coefficients. However, the ice grains are usually not spherical even though statistically the ice is spherically symmetric. Whether or not one is inclined to ignore these difficulties, it is undeniable that radiative transfer theories for example have led to predictions of unacceptably low brightness temperatures for dry snow at sufficiently high frequencies (Stogryn 1986).

Among the approaches not based on radiative transfer the strong fluctuation theory is among those which have led to the best results when trying to reproduce experimental parameters of sea ice signatures. The model of Stogryn (1987) in the implementation of Grenfell describes the emissivity of an isothermal sea ice layer in the microwave region between 1 and 100 GHz. It is based on the many–layer–strong–fluctuation–theory, a self–consistent theory relying on the Maxwell equations. The sea ice consists (in view of the model) of isothermal layers of snow and ice. For each of them different parameters are defined to describe its structure and constituents. The layer structure is used to calculate the dielectric properties and the emissivity of the sea ice. Under the layers of the ice the model needs an optically thick layer, normally water or thick ice.

Open Ocean Module

The three scale model for the ocean surface used for the combined model gives the opportunity to calculate the bistatic scattering coefficient matrix (surface scatter matrix) of a wind–roughened, foam–covered ocean surface in a mainly analytical way (Schrader 1997). The first scale describes hydrodynamical waves with a radius of curvature larger than the wavelength of the electromagnetic waves. These are mostly gravity waves. The formalism to calculate the scattering coefficients of such a surface is given by the *Kirchhoff*–model, assuming specular reflection on the inclined portions of the waves (facet model), weighted by the probability of the occurence of the slopes.

Due to the statistical character of the approach of the *Kirchhoff*– model, the probability distribution function is expressed by the slope variances. These are calculated from the wave spectrum described by the model of Bjerkaas and Riedel (1979). The slope variances are determined by parametrizations calculated from the wave spectrum in dependence of the friction velocity and observation frequency. The second scale is given by the short

waves, which remain in the wave spectrum if the waves of the first scale are removed. These are typically the very short gravity waves and the capillary waves.

The first and second scale are separated by the cutoff wavenumber, which is determined in dependence of the frequency and the surface stress. The value is choosen in order to satisfy the assumption of both models. The scattering behaviour of the second roughness scale is calculated by an approximation of the small pertubation method, which assumes the small scale part as a perfect reflector. Thus no polarization effects are taken into account. The roughness parameter of this scale is the variance of the amplitude of the small scale waves which are determined from the wave spectrum. The scattering due to the small scale roughness scale leads to a modification of the Fresnel–coefficients, which describe the reflectivity of each facet.

The third scale is incorporated by the changes in reflectivity due to whitecaps and foamstreaks, which are separately considered. The third scale is assumed to occur on each facet and modifies the reflection coefficient of the facet. A normalization in the integration procedure of the first scale leads to an exact treatment of the mathematical problem. The reduction in reflectivty due to shadowing effects is incoperated. Multiple scattering is considered by an approximated and efficient approach, which takes the mainly geometrical effect of multiple scattering into account (Guissard and Sobieski 1987).

Atmosphere Module

The radiative transfer in the atmosphere is generally described by the equation of radiative transfer. Various methods for the numerical solution of this equation have been developed. The gaseous absorption of oxygen and water vapour in the atmosphere is the most important process and is calculated with the millimeter wave propagation model of Liebe et al. (1992). The attenuation by clouds and precipitation are modelled by Mie–theory. The numerical solution of the equation of radiative transfer equation is performed with the 'successive order of scattering' method. The radiative coupling to the surface, open or sea ice covered ocean, is done by reflectivities and emission temperatures supplied by the corresponding surface models.

Validation of the Combined Model

To validate the combined microwave model, brightness temperatures are simulated according to the observed synoptic situation and are compared to observed SSM/I data for six test cases. These test cases have been composed from data taken during research expeditions experiments ARKTIS'88 and ARKTIS'93 in the Fram Strait (Fig. 1). To

reduce possible effects of geolocation errors of the SSM/I pixels, as well as to minimize the influence of horizontal inhomogeneities of the scene, the 10 nearest SSM/I observations (with respect to the lower frequency channels) are averaged.

For the evaluation it is not expected to find an exact agreement between observed and simulated brightness temperatures. Differences in the order of a few Kelvin have to be expected, which may originate from an insufficient simulation or SSM/I instrument errors, as well as the above mentioned scene errors. The general strategy for the evaluation is to simulate brightness temperatures for varying environmental conditions (e.g. cloud free, cloudy, partially ice covered ocean, ...) according to the synoptic observations. The validation is judged successful, if the simulated brightness temperatures are close to the observed ones. The interpretation of 'close' depends on the synoptic conditions observed. The acceptable difference between the simulated and observed brightness temperatures is taken as the sum of the absolute error (3 K) of the SSM/I instrument and the standard deviation of the observed brightness temperature(2–3 K). Hence the differences should not exceed an absolute value of 5 to 6 K.

Case 1 was located far from the ice edge and no sea ice was present, the other cases were located within the ice field. However, these cases are not independent. Cases 2 to 4 were located on the same ice floe, cases 5 and 6 on another floe. While cases 2 to 4 were observed during the winter season at very low temperatures, the data for the cases 5 and 6

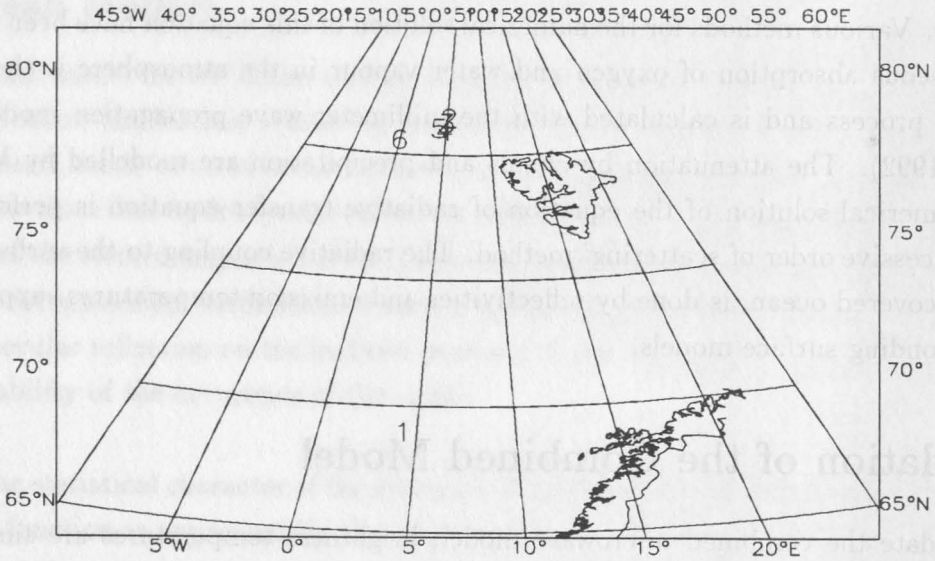

Figure 1 Locations of test cases indicated by numbers.

Table 1 Summary of differences between observed and simulated brightness temperatures of all test cases using the simulations with the best overall agreement. For test case 1 results of the 3– scale model and of the Wisler and Hollinger parameterization (W&H) are presented. The differences for test case 4 include the simulations for the extended sea–ice covered pixel (85 %) and the 'open water' pixel (65 %).

channel	case 1		case 2	case 3	case 4		case 5	case 6
	3–scale	W&H			85 %	65 %		
19 v	-4.8	-5.0	-1.2	2.2	-1.2	-0.7	-1.7	-5.3
19 h	-3.7	0.5	3.2	3.8	1.1	5.8	4.0	0.4
22 v	-0.9	2.1	2.0	4.8	1.1	2.9	0.8	-2.2
37 v	-2.9	-0.3	12.8	13.6	9.6	9.9	27.6	10.0
37 h	4.3	0.2	13.3	11.7	8.5	14.6	15.9	5.4
85 v	3.2	1.2	5.2	-0.4	-0.9	2.3	2.0	7.1
85 h	2.2	-3.7	5.6	-1.4	-2.3	0.7	0.3	-3.3

have been measured during spring with temperatures just below the freezing point. Thus large differences in the ice structure between the two subsamples may exist due to melting and refreezing processes.

The differences between the observed SSM/I brightness temperatures and the closest simulation results are given in Tab. 1 for all cases. Case 1 one was used to evaluate the ocean module with two approaches to estimate the effect of the surface roughness: the 3–scale model and the parameterization by Wisler and Hollinger (1977). The latter formulation yields a somewhat better overall agreement with the observed brightness temperatures. However, due to the strong influence of the clouds and the fact that the actual liquid water content is unknown, it is not possible to give a preference to one of both methods. To do this, simulations for cloud free observations for more than one test case have to be analyzed.

The simulations for the test cases with sea ice show large deviations for the 37 GHz channels, while the differences between observed and simulated brightness temperatures for the other channels are within the acceptable range. Taking into account that the standard deviations for test case 6 are higher than for the other cases, the difference of 7.1 K at 85 GHz vertical polarization is also acceptable. To achieve an agreement between observation and simulation it is important to consider the sea ice concentration and the amount and phase of cloudiness. Especially for snow clouds the influence at 85 GHz is very significant. The source for the large deviations at 37 GHz are thought to origin-

ate from the sea–ice module, because they do not appear for the open ocean simulation (case 1). A change of the sea–ice input parameters may improve the simulations, but to select appropriate values a detailed sensitivity analysis is needed. However, the actual reason for this shortcoming of the sea–ice module is unknown, but a possible explanation is the absence of surface scatter in the module. Another error source is that the calculated emission from the ice surface is based on the net reflection only and prescribed emission temperature. The actual emission may originate from deeper layers than the surface with different emissivities and temperatures.

Sensitivity Analysis

The task of the sensitivity analyses is the estimation of changes in brightness temperatures due to changes of environmental parameters. Therefore those parameter changes, which show the most prominent effect on the radiative signal, should be investigated. On the other hand, the variation of the parameters has to be within the limits of the natural occurance. For instance, a precipitable water content of 50 kg m^{-2} will not be found in polar regions. The brightness temperature observed from space is a composed signal from the atmosphere, the open ocean, and the sea ice covered ocean. Thus the most effective parameters of each of these subenvironments have to be considered.

From the validation analysis an error of the sea ice reflectivity at 37 GHz became obvious. To achieve a more reliable sensitivity study a correction has been estimated on the basis of the observations from test case 2. This case is suitable because no clouds have been observed and thus a cloud free atmosphere can be assumed, which omit errors due to atmospheric hydrometeors. The correction factors for the sea ice surface reflectivity at 37 GHz have been estimated to 2.0 and 1.5 for the vertical and horizontal polarization, respectively. This correction brings the observed and simulated brightness temperatures of the test cases into close agreement.

The sensitivity analyses of the individual environments (open ocean, sea ice, atmosphere) demonstrate the influence of a single parameter to the brightness temperatures. In the view of a combined environment the relevance of a single parameter compared to the other is estimated and given in Tab. 2. The strongest changes of the brightness temperatures are caused by a change of the sea ice concentration, assuming a variation from 0 to 100%. The effects of the other surface parameters (sea ice parameters and wind speed) strongly depend on the sea ice concentration and have to be weighted with this quantity.

The effects of atmospheric hydrometeors also depend on the sea ice concentration. They are most pronounced over the open ocean and reduced effects are found for a fully sea ice covered ocean, due to the large emissivity of the sea ice. The influence of the atmospheric

hydrometeors on sea ice retrievals, which use the polarization (PR) and gradient (GR) ratios (e.g. NASA sea ice algorithm), is shown in Fig. 2. The tie–points for open water (OW), first–year ice (FY), and multiyear ice (MY) are also drawn for orientation purpose. Simulations for rain and snow clouds with varying water content have been carried out for open water (wind speed=10 m/s) and a fully ice covered ocean, marked by (+) and (∗), respectively. The PR and GR values for the cloud free situation are marked by 'L'. For rain clouds over open ocean GR is always larger than the open water threshold of 0.05; thus no effect on the sea ice retrieval results. For a sea ice covered ocean increasing water content of rain clouds correspond to a shift from multiyear ice to first–year ice. The total sea ice concentration (the distance to the open–water tie point OW) is only slightly effected. In contrast to rain clouds, an increasing water content of snow clouds is equivalent to a shift from first–year ice to multiyear ice and slightly increases the total ice concentration retrieval. Over open water heavy snow clouds will interpreted as sea ice. With increasing wind speed GR also increases, but PR decreases. Thus over open water the sea ice retrieval is not effected. However, over partially sea ice covered ocean an increasing wind speed corresponds to an increase of the total ice concentration and a shift from multiyear ice to first–year ice. By the effects discussed above it is obvious that the atmospheric state significantly effects the retrieval of sea ice, if not taken explicitely into accounted.

Table 2 Relevance of variations of physical parameters on brightness temperatures: very important (+++), important (++), less important (+). The effects of parameters (except ice concentration) strongly depend on the sea ice concentration; the relevance is estimated for an ice cover of about 50%. Other parameters are of less significance and have been omitted.

parameter	importance
sea ice concentration	+++
snow clouds	++
rain clouds	++
clouds liquid water	++
wind speed	++
snow free water fraction	++
snow density	++
snow grain diameter	++
ice density	+
ice salinity	+
air bubble diameter	+

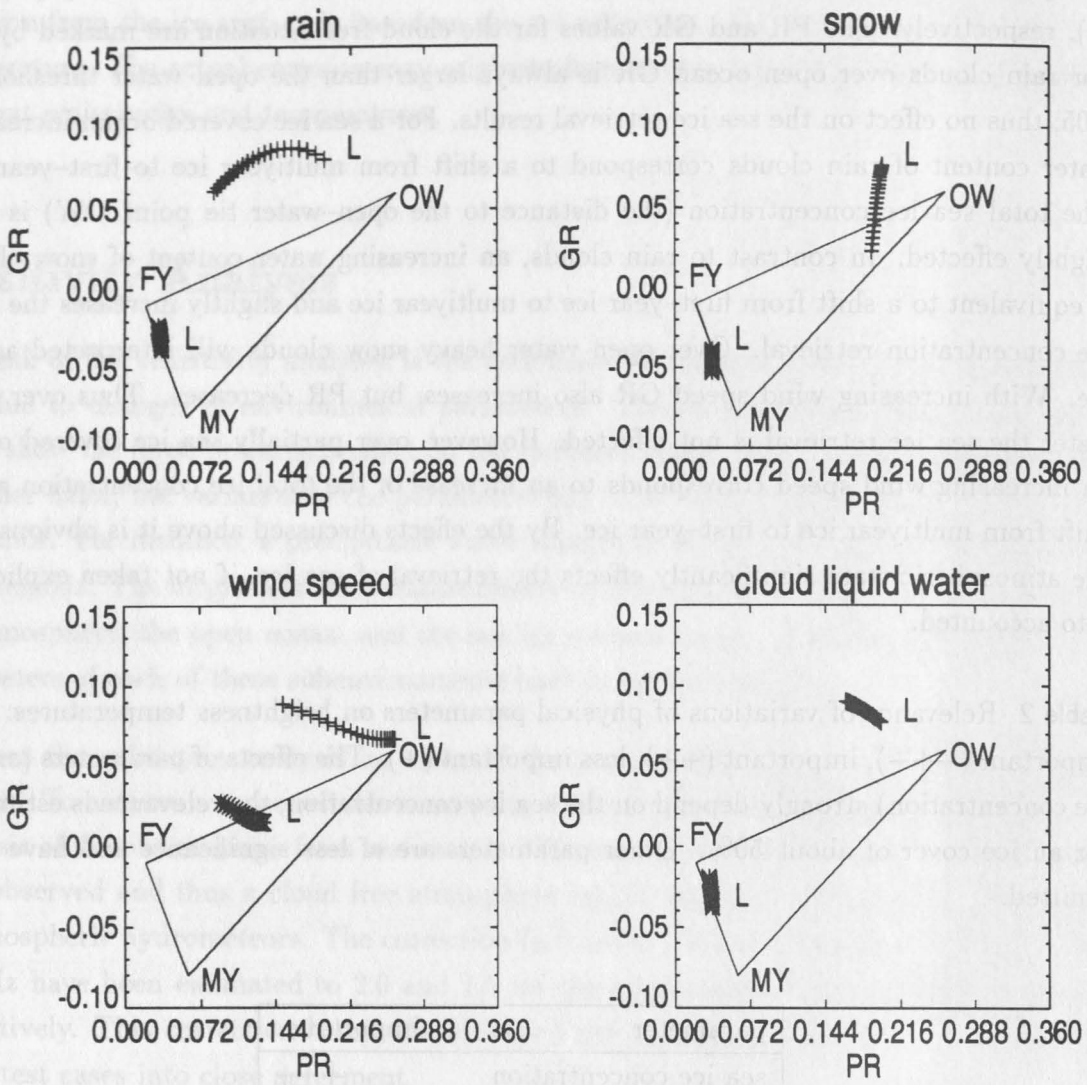

Figure 2 Variation of the polarization (PR) and gradient (GR) ratio induced by the variation of large–droplet clouds (rain) (0 – 0.4 kg m^{-2} LWP), snow clouds (0 – 0.4 kg m^{-2} LWP), wind speed (0 – 25 m/s), and sea ice concentration (0 – 100%). Simulations represent the open ocean (+) and totally sea ice covered ocean (∗) for rain and snow clouds, and cloud liquid water (LWP); open ocean (+) and half sea ice covered ocean (∗) for wind speed.

Retrieval Algorithms

A principal application of the combined model is the use for the develpoment of retrieval algorithms. The simulated brightness temperatures, including a wide variety of geophysical parameter combinations, have been related to the geophysical parameters using a neural network approach. Algorithms for the sea ice concentration, wind speed and atmospheric cloud parameter have been derived and tested against independent observations. The retrieved sea ice concentration is similar to the NASA tie point algorithm estimates, and differences are thought to originate from atmospheric clouds and wind speed effects. The wind speed estimates using the neural network algorithm is in agreement with synoptic observations. From the fitting results of the neural network it is estimated that the wind speed retrievals are reliable up to 70 % ice coverage. While for liquid water and snow clouds the estimated water path corresponds to the synoptic observations, the results from the rain cloud retrieval are not. However, there are no direct cloud water measuremnts available.

So far the developed algorithms should be treated as a first step and there is a large potential for further improvements. The neural network configuration can be optimized and the number of simulated brightness temperatures as well as their quality can be increased.

Summary

In this study a microwave radiative transfer model for polar regions has been developed. This model will help to improve the qualitative understanding of the radiative properties of the ice covered surface and atmosphere. The validation of the model exhibited shortcomings for the 37 GHz frequencies, which originate from the sea ice module. The reasons for this are unknown and need further investigations. A possible error source is the artificial oscillation of the sea–ice reflectivity as function of frequency and ice–layer thickness. Despite this problem the simulated reflectivities for different ice types (new ice, first–year ice, and multiyear ice) show a good agreement with measurements for the horizontally polarized emissivity. The simulated vertically polarized emissivity is a about 0.05 too low.

However, an empirical correction for the 37 GHz frequencies allowed a detailed sensitivity study and advanced retrieval. The sensitivity analysis demonstrated the effects of the individual parameters on the total signal. Especially the influence of atmospheric hydrometeors on the satellite received signal is of importance for sea ice retrievals. The application of the combined model to retrieval algorithm development gives promising results and allows the inclusion of atmospheric and open ocean effects explicitely.

References

Bjerkaas, A. W. and F. W. Riedel, 1979: Proposed Model for the Elevation Spectrum of a wind–roughened Sea Surface. *Technical Memorandum*(JHU/APL TG 1328), 31.

Guissard, A. and P. Sobieski, 1987: An approximate Model for the Microwave Brightness Temperature of the Sea. *International Journal of Remote Sensing*, **8**(1), 1607–1627.

Liebe, H. J., P. W. Rosenkranz, and G. A. Hufford, 1992: Atmospheric 60–Ghz oxygen spectrum: New laboratory measurements and line parameters. *J. Quant. Spectrosc. Radiat. Transfer*, **48**, 629–643.

Schrader, M. and E. Ruprecht. A Three–Scale–Model to Calculate the Reflectivity of a Windroughened, Foamcovered Sea Surface in the Microwave Frequency Range, 1997. *submitted to JGR.*

Stogryn, A., 1986: A Study of the Microwave Brightness Temperature of Snow from the Point of Strong Fluctuation Theory. *IEEE Transactions on Geoscience and Remote Sensing*, **GE–24**(2), 220–231.

Stogryn, A., 1987: An Analysis of the Tensor Dielectric Constant of Sea Ice at Microwave Frequencies. *IEEE Transactions on Geoscience and Remote Sensing*, **GE–25**(2), 147–158.

Wisler, M. M. and J. P. Hollinger, 1977: Estimation of Marine Environmental Parameters Using Microwave Radiometric Remote Sensing Systems: Technical Report NRL Memo. Rep. 3661, Naval Research Laboratory, Washington, D.C.

Contents

1 Introduction **5**

2 Review and Selection of Models **8**

2.1 Sea Ice Emissivity Models 8
2.1.1 Physical Emissivity–Models for Sea Ice 9
2.1.2 Radiative Transfer Theories 10
2.1.3 Strong Fluctuation Theories 12
2.1.4 Major gaps and recommendations 14
2.2 Open–Ocean Models 15
2.2.1 Physical Background 15
2.2.2 Surface Reflection Models 16
2.2.3 Three Scale Models 18
2.2.4 Consideration of Foam 19
2.2.5 Environmental Conditions 20
2.2.6 Recommendation for Oceanic Model 23
2.3 Atmospheric Models 24
2.3.1 Solutions of the Radiative Transfer Equation 25
2.3.2 Accuracy of Models 30
2.3.3 Three Dimensional Transport 30
2.3.4 Molecular Absorption 30
2.3.5 Attenuation by Clouds and Precipitation 33
2.3.6 Cosmic Background Radiation 35
2.3.7 Recommendation for Atmospheric Model 35
2.3.8 Review of Environmental Conditions 36
2.3.9 Identified Gaps and Recommendations 37
2.4 Surface-Atmosphere Interactions 37
2.4.1 Atmospheric Impact on the Ice Microphysics 37
2.4.2 Radiative Surface–Atmosphere Interactions 41
2.4.3 Azimuthal Dependence 45
2.5 Selection Criteria and Selection of Models 45
2.5.1 Sea Ice Model 45
2.5.2 Free Ocean Model 47
2.5.3 Atmospheric Model 48
2.6 Atmospheric Impact on the Ice Microstructure 50
2.6.1 Introduction 50
2.6.2 First–Year Ice 50
2.6.3 Multiyear ice 54
2.6.4 Snow 57

2.6.5 Conclusion 71

3 Combined Model **75**

3.1 Sea–ice Module 75

3.1.1 Introduction 75

3.1.2 The Layer Structure of the Model 78

3.1.3 Some results of the ice–module 81

3.2 Free–Ocean Surface Module 86

3.2.1 Description 86

3.2.2 Model Structure 87

3.2.3 Input parameter 87

3.2.4 Output parameter 87

3.3 Atmospheric Module 89

3.3.1 Selection of Code 89

3.3.2 Successive Order Scattering Method 89

3.3.3 Verification and Validation 91

3.4 Programme Structure of the Combined Model 92

3.4.1 Introduction 92

3.4.2 The General Layout of MWMOD 95

4 Model Validation **99**

4.1 Review of Test Cases 99

4.1.1 ARKTIS'88 100

4.1.2 ARKTIS'93 101

4.1.3 Selection of cases 102

4.2 Ground Truth Requirements 104

4.2.1 Sea Ice Parameters 104

4.2.2 Atmospheric Parameters 106

4.2.3 Open Ocean Parameters 106

4.3 Case 1: Free ocean, partly clear atmosphere, winter 106

4.3.1 Synoptic Situation 106

4.3.2 Atmospheric Parameters 107

4.3.3 SSM/I Observations 108

4.3.4 Validation 108

4.4 Case 2: Ice, small cloud fraction, winter 116

4.4.1 Synoptic Situation 116

4.4.2 Atmospheric Parameters 116

4.4.3 Surface Parameters 117

4.4.4 SSM/I Observations 118

4.4.5 Validation 121

4.5 Case 3: Ice, overcast sky, winter 126
4.5.1 Synoptic Situation 126
4.5.2 Atmospheric Parameters 126
4.5.3 Surface Parameters 128
4.5.4 SSM/I Observations 134
4.5.5 Validation 134
4.6 Case 4: Ice, partly cloudy sky, winter 139
4.6.1 Synoptic Situation 139
4.6.2 Atmospheric Parameters 139
4.6.3 Surface Parameters 141
4.6.4 SSM/I Observations 141
4.6.5 Validation 142
4.7 Case 5: Ice, overcast sky, spring 154
4.7.1 Synoptic Situation 154
4.7.2 Atmospheric Parameters 154
4.7.3 Surface Parameters 156
4.7.4 SSM/I Observations 156
4.7.5 Validation 162
4.8 Case 6: Ice, overcast sky, spring 162
4.8.1 Synptic Situation 162
4.8.2 Atmospheric Parameters 164
4.8.3 Surface Parameters 164
4.8.4 SSM/I Observations 166
4.8.5 Validation 171
4.9 Summary and Discussion 173

5 Sensitivity Analysis **177**
5.1 Definition of Sensitivity Parameters 177
5.1.1 Open Ocean 177
5.1.2 Ice Coverd Ocean 177
5.1.3 Atmosphere 178
5.2 Sensitivity to Surface Parameters 179
5.2.1 Open Ocean 179
5.2.2 Sea Ice 180
5.3 Sensitivity to Atmospheric Parameters 194
5.4 Summary 195

6 Retrieval Algorithms **198**
6.1 Introduction 198
6.2 Algorithm Development and Application 199

6.3 Summary 201

7 Conclusion and Recommendations **203**
7.1 Judgement of Model Performance 203
7.2 Recommendations 206

A Backus–Gilbert Inversion **209**

B MWMOD Control Parameters for Validation **213**
B.1 Case 1 213
B.2 Case 2 215
B.3 Case 3 217
B.4 Case 4 219
B.5 Case 5 221
B.6 Case 6 223

C References **225**

1 Introduction

With the advent of more powerful computers and the considerable progress achieved in recent years in the modeling of the atmosphere and the ocean — the two of the most important components of the climate system — it may be expected that a major thrust in climate research will be directed in the future towards a better understanding and modeling of the coupled ocean–atmosphere system. This is particular important in polar regions where in addition sea ice affects the ocean/atmosphere heat exchange by cutting off the turbulent flux exchanges and reflecting a large percentage of sunlight. This influences in a massive way both, the polar atmosphere and the deep water formation.

Sea ice, which occupies between 5% (March) and 8% (September) of the world ocean, plays in the world climate system the role of an energy sink. Furthermore, a change of the sea ice cover influences by the exchange of momentum and heat between ocean and atmosphere and by freezing and melting processes the global circulation of ocean and atmosphere (Barron and Battrick 1991). Knowledge of the wintertime distribution of open water and ice thickness across the ice–covered polar seas is critical to our understanding of polar ocean processes and the role of polar regions in the global climate system. Energy exchange between ocean and atmosphere is controlled largely by the occurrence of openings in the ice pack and areas of new and young ice. The importance of determining the distribution of these ice types is clear from modeling results, which suggest that heat input to the atmosphere over ice of less than 0.4 m thickness is between 1 and 2 orders of magnitude greater than over ice of a meter or more in thickness (Maykut 1978). Additionally the absence of leads (lead fraction) would increase the mean temperature of about 3 K (Ledley 1988).

Our ability to quantify with sufficient accuracy the rates of heat loss and related processes is limited in part by our inability to accurately determine the distribution of open water, new ice, and young ice (Cavalieri 1994). Sea ice cover is an important indicator for changes of the global climate (Lemke 1987). Therefore it is highly desirable to improve the (practically exclusively) remote sensing methods for sea ice cover, thickness and type. The most important tool of observing sea ice are passive microwave measurements. They are almost continuously available with a global coverage since over 30 years (Tab. 1). They are independent of the solar illumination and (approximately in the lower frequencies) weather conditions.

To gain and improve the understanding of sea ice signatures on disparate scales, passive microwave research has been conducted over the past two decades using sensors located on the ice surface, in aircraft flying at a range of altitudes, and onboard of satellites in space. Early work, which used data obtained mainly from aircraft and satellite sensors,

Table 1 Satellites and radiometers with ice monitoring capabilities.

Satellite	Sensors	Usable Time Periods
Cosmos–243		09/1962
Cosmos–384		12/1970
Nimbus–5	NEMS	10/1972 – 1975
	ESMR	12/1972 – 03/1980
Nimbus–6	SCAMS	06/1975 – 03/1976
	ESMR	06/1975 – 09/1976
Meteor–series		since 1978
Seasat	SMMR	06/1978 – 10/1978
Nimbus–7	SMMR	10/1978 – 06/1987
MOS–1	MSR	since 02/1987
DMSP–F8	SSM/I	06/1987 – 12/1991
DMSP–F10	SSM/I	since 12/1990
DMSP–F11	SSM/I	since 12/1991
DMSP–F12	SSM/I	since 10/1994
ERS–x	MIMR	(2000)

established that the three dominant surfaces in the Arctic, open water, first-year ice and multiyear ice, could be discriminated from each other on the basis of their contrasting radiometric signatures. These observations laid the groundwork for operational algorithms now used to derive ice concentration information from satellites (Eppler et al. 1992).

Sea ice retrieval with passive microwave sensors on satellites has mostly regarded the atmospheric contribution as inevitable, but neglectable noise. Only some recent work takes account of the atmosphere by introducing appropriate corrections. Retrieval of atmospheric parameters from satellites over the oceans has an equally long tradition as ice retrieval both starting with the only two weeks lasting measurements of the USSR satellite Cosmos–243 in 1962 (Tab. 1, see also Basharinov et al. 1971; Mitnik 1974). A wealth of algorithms have been derived for total water vapor content, cloud liquid water, rain rate, and near-surface windspeed. The philosphy of the taken approaches aims at minimizing effects of the underlying surface. This works satisfactorily for the free-ocean surface due to the low emissivity which reduces the signal of the surface, due to the compensating effects of sea surface temperature and sea water emissivity on the effective radiation temperature of the ocean surface, and due to the common choice of viewing angles around 50° which minimizes roughness effects on the vertically polarized emissivity. The emissivity of ice surfaces does not offer these advantages. The ice dominates the signal and the retrieval quality of atmospherical parameters is largely reduced.

At the described point of passive microwave research, where atmospheric and surface retrievals are well developed, but consider each other as disturbances, the time seems mature to establish an integrated surface and atmosphere retrieval. For example, variations in ice temperature, wind speed (over open water) and atmospheric water content cause variations in passive microwave signatures that look like noise in averaged data, but are at least partly invertible. Thus, sea ice microwave signatures contain more geophysical information than is routinely utilized; much of the potential of sea ice microwave remote sensing remains untapped (Winebrenner et al. 1992).

The first logical step towards this goal is to develop an integrated model for surface emission and radiative transfer in the atmosphere. Sea ice and open water are particularly suited candidates for such an integrated model because they exhibit only a small number of surface types and parameters. For land surface, there are much more different surface types, and they vary on a much smaller scale.

2 Review and Selection of Models

2.1 Sea Ice Emissivity Models

Formation of sea ice is a complex process. The initial sea ice types differ according to the meteorological conditions during the formation process, as described by Weeks (1976) diagrammatically, see Fig. 1. The definition of the ice types shown there has been motivated from the visual appearance. It has been overtaken by the WMO (1989).

To date, operational microwave remote sensing of sea ice has been based primarily on empirical relations between signatures and ice types or ice concentrations. Empirical remote sensing has proven valuable in many geophysical studies, but a reliance on em-

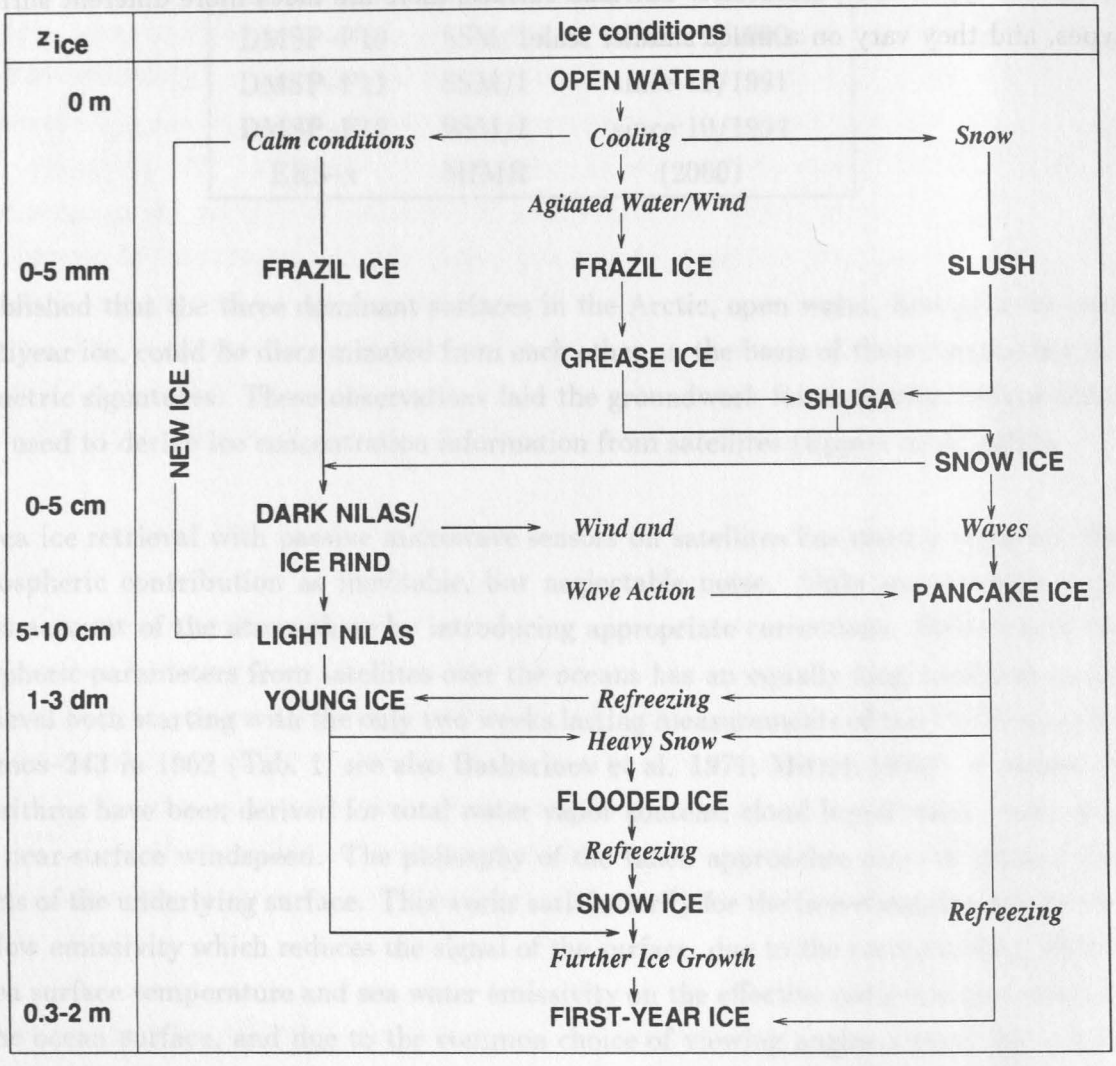

Figure 1 Evolution of new sea ice (adopted from Weeks 1976); ice types are given in bold letters, the related environmental processes are shown in italic letters.

piricism alone severly limits realization of the potential value of remote sensing methods (Winebrenner et al. 1992).

The passive microwave signature is determined by the electromagnetic properties of the sea ice. There exist a lot of different kinds of sea ice, which have different electromagnetic properties. The layered physical model of sea ice (Fig. 2) is common to most sea ice models. Note that old ice contains many relatively large air bubbles in the upper layers and first-year ice contains many brine pockets at all depths, but relatively small air bubbles.

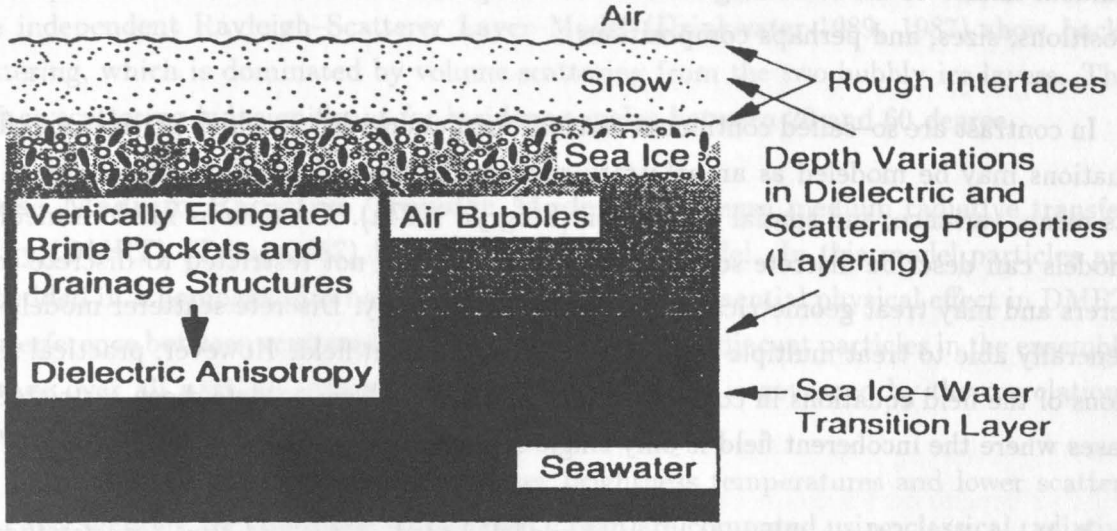

Figure 2 Layered physical model of sea ice (adopted from Winebrenner et al. 1992).

2.1.1 Physical Emissivity–Models for Sea Ice

The first issue is whether a model derives signatures based on scattering from dielectric inhomogeneities within the medium alone (volume scattering), scattering only from roughness at interfaces in the medium (rough surface scattering), or from some combination of the two. Rough surface scattering models are presently fewer in number and they calculate as the most important quantity the backscattering coefficient. On the other hand volume scattering models allow to calculate the emissivity which is necessary in the combined model. We therefore restrict the discussion to volume scattering models.

Ice properties typically show pronounced variations with depth and snow may cover the ice. Signature models typically treat the air-snow-ice-seawater system as a stack of horizontal layers with planar or rough surfaces. Models differ significantly in the number of scattering layers they treat (Lee and Kong 1988; Stogryn 1985). When layer interfaces are nearly planar (measured in radiation wavelengths) and scattering in the layer is

not too strong, waves reflected from layer interfaces remain coherent and thus interfere. Most models treat field contributions as either completely coherent (e.g. strong fluctuaion theories (Stogryn 1987)) or completely incoherent (e.g. classical radiative transfer models (Tsang et al. 1985)).

Another distinction between volume scattering models arises in the way they picture the spatial permittivity fluctuations inside the scattering medium. Discrete scatterer models envision a homogeneous background medium in which are embedded discrete inclusions or particles of materials having permittivities different from that of the background. The random nature of the scattering medium in this picture is due to randomness in particle positions, sizes, and perhaps compositions.

In contrast are so–called continuous random medium models in which permittivity fluctuations may be modeled as an arbitrary random function of position, characterized by its mean, variance, and spatial correlation (Stogryn 1984a). Continuous random medium models can describe discrete scatterers too, but they are not restricted to discrete scatterers and may treat geometrically complex media directly. Discrete scatterer models are generally able to treat multiple scattering of the incoherent field. However, practical solutions of the field equations in continuous medium models have, to date, been restricted to cases where the incoherent field is only single scattered.

A discussion of three different kinds of models based on the *radiative transfer theory*, and three models based on the *strong fluctuation theory* is given below.

2.1.2 Radiative Transfer Theories

The fundamental quantity in radiative transfer (Ishimaru 1978) is the spectral radiance L defined at any point in space r as the power flowing in a given direction $\vec{s}$ per unit solid angle per unit emitting area per unit bandwidth. Radiative Transfer theories assume unpolarized radiation and the models use spheres as scatterers. The diameter of the scatterers is lower than the radiation wavelength. The classical theory is based on the radiative transfer equation

$$\frac{dL(r,\vec{s})}{d\vec{s}} = -k_e L(r,\vec{s}) + \int_{4\pi} d\vec{s}' P(\vec{s},\vec{s}') L(r,\vec{s}') + J(r,\vec{s}) \qquad (1)$$

where k_e is the extinction coefficient, P is the so-called phase function relating scattering from direction $\vec{s}'$ into direction $\vec{s}$, and J is a thermal source term owing to emission within the scattering volume. This equation describes the total change in specific intensity in the direction $\vec{s}$ as a sum of effects, namely extinction, scattering from other directions into the direction $\vec{s}$, and thermal emission into that direction.

The classical theory was developed to treat cases where scatterers occupied less than 1% of the total scattering volume. The scattering particles in snow and sea ice typically occupy 5 to 50% of the scattering volume; effects of one scatterer on the contribution of another can therefore become appreciable. Such effects are generally termed dense medium effects.

Independent Rayleigh-Scatterer Layers The model consists of two bubbly ice layers overlain by dry snow. The layers have a constant thickness. The scatterers are assumed uniformly distributed within each layer. The layer densities and the distribution of the sphere radii are to be specified from ice and snow characterization data.
The model does not presently treat any effect of dielectric anisotropy in congelation ice. The independent Rayleigh–Scatterer Layer–Model (Drinkwater 1989, 1987) show back-scattering, which is dominated by volume scattering from the two bubbly ice layers. The surface scattering is insignificant for incidence angles between 20 and 60 degree.

Dense Medium Radiative Transfer Model The dense medium radiative transfer theory (DMRT) (Tsang 1987) is a discrete scatterer model. In this model particles are embedded in a homogenuous background medium. The essential physical effect in DMRT is interference between scattered field contributions from adjacent particles in the ensemble average over all particle arrangements. The interference is governed by the correlations between particle positions.
For a given set of input parameters, higher brightness temperatures and lower scattering cross sections are computed using DMRT than are computed using classical radiative transfer theory. This theory is fully polarimetric. To construct it, the scalar radiance L is generalized to a vector quantity $\mathbf{L}$ whose components are the four Stokes parameters of the wave at r propagating in direction $\vec{s}$. The interference between waves reflected from various layer interfaces is neglected.
The model which is used in the test consists of two scattering layers overlying a homogeneous nonscattering medium. Particle shapes in the present theory (Tsang and Ishimaru 1987) and implementation are restricted to spheres, and sizes are presently limited to the regime in which Rayleigh scattering is valid. The spherical particles restriction precludes modeling of any effects of dielectric anisotropy in the ice; thus DMRT is likely to be most appropriate in old ice or other ice that is dielectrically isotropic. The model shows a small sensitivity to salinity and a very small sensitivity to layer thickness and density.

Dense Medium Theory The Dense Medium Theory (Fung and Eom 1985) is also a discrete scatterer model for spheres much smaller than the radiation wavelength. The essential physical difference between dense medium theory and the classical theory is the modification of the phase matrix, and therefore also the extinction coefficient. Classical radiative transfer uses the Rayleigh scattering phase matrix for small spheres. Fung and Eom (1985) rederived the phase matrix using Mie coefficients for terms in the spheres'

fields that fall off in range faster then $1/r$ (r = radius). The total scattering cross section is computed by integrating the modified phase function over all solid angles, then added to the absorption cross section from Lorenz-Mie theory to obtain the extinction coefficient. The dense medium theory predicts an increase in scattering over that computed from the classical theory. Snow brightness temperatures (7–10 GHz) are 1–8 K lower than classical values.

2.1.3 Strong Fluctuation Theories

The term strong fluctuation theory (SFT) (Stogryn 1985) refers to a class of volume scattering models that employ the continuous random medium model to describe the scattering medium and address the problem of strong contrasts in the permittivity of constituents of the scattering medium (Tsang et al. 1985).
The correct treatment of such contrasts requires decomposition of integrals involving the dyadic Green's function for the electric fields into sums of two terms. One term is the principal value integral with the volume around the source point excluded. The shape of this exclusion volume is determined by the shape and orientation of the scatterers and/or equicorrelation surfaces of the random permittivity. So it is possible to describe aspherical scatterers with this theory. The second term consists of an integral over a product of terms, including a delta function centered on the source point times a dyad of which elements depend on the shape of the exclusion volume (Stogryn 1983b).
The theory is based on a bilocal approximation (Stogryn 1983a, 1984b) and uses the distorted Born approximation. Emissivities are calculated on the basis of Kirchhoff's law.

Polarimetric Strong Fluctuation Theory In the polarimetric SFT, the strong permittivity fluctuations due to individual brine pockets or air bubbles are directly responsible for volume scattering within the sea ice (Nghiem 1991). The individual scatterer are ellipsoidal particles of identical size. Thus it is possible to model the brine pockets in sea ice. In snow spheres are used (this shows the isotropy of typical snow). The spatial distribution of scatterer locations within the layers is uniform.
The theory shows a quantitative agreement with the measurements similar to the many layer strong fluctuation theory. There is a minor role for scattering for the passive signatures. The reflectivities of the ice sheet determined by the mean permittivity govern the emissivities.
The theory shows a better agreement for 37 GHz horizontal polarization than the many layer strong fluctuation theory. But passive signature results are insensitive to the choice of the correlation length of the brine pockets. The theory calculates emissivities at higher frequencies (90 GHz) too low.

Modified Radiative Transfer Theory The Modified Radiative Transfer Theory (MRT) is a model in the general form of classical radiative transfer based on the continuous random medium model (Lee and Kong 1988; Mudaliar and Lee 1990). The permittivity fluctuations may be strong. The MRT computes the coherent field using the nonlinear approximation in Dyson's equation (Tsang et al. 1985). The Dyson's equation calculates the mean value of the dyadic Green's function (DGF) using an infinite Neumann series for the DGF. The bilocal approximation of the strong fluctuation theory assumes that the coherent field travels between scattering events with the propagation constant appropriate for the background ice. By contrast, the nonlinear approximation assumes a propagation constant equal to the effective propagation constant of the sea ice, and thus accounts for additional multiple forward scattering events in the coherent field.
The MRT makes use of the general Bethe-Salpeter equation for the incoherent field and the latter approximation for the intensity–operator in this equation. It is a self–consistent theory in terms of energy–conservation. Including some multiple scattering of the incoherent field would seem to permit MRT to treat stronger scattering than theories using the distorted Born approximation (Winebrenner et al. 1992).

However, solution of the nonlinear approximation equation for the coherent field remains restricted to the low–frequency regime. The net effect of this restriction is not presently clear. The solutions of the theoretical equations to date are restricted to a single, infinitely thick scattering layer; the only layer–interface is at the top of the layer. Thus there can be no interactions of waves from different layers. The physical model which is used for the ice has not an ice–water interface and the ice properties doesn't vary with depth. Dielectric properties are modeled as directionally anisotropic, however, with a specified tilt direction for the (single) preferred direction. Thus the tilt direction, as well as mean permittivities, normalized variances of permittivity and permittivity correlation lengths, in directions parallel and perpendicular to the preferred direction, must be specified directly. The most sensitive parameters in computing backscattering cross sections are the imaginary parts of the mean permittivities and the permittivity correlation length.
Predictions at vertical polarization, with the exception of 10 GHz, show good agreement even at 90 GHz. The present solutions are limited to first-order scattering. The model predicts no feature at 10 GHz like the many layer strong fluctuation theory.

Many Layer Strong Fluctuation Theory Stogryn has developed a model also based on strong fluctuation theory, but which is substantially different from that described above (Stogryn 1983a, 1983b, 1984a, 1984b, 1985, 1987). The theory treats problems with many layers (over 30 are possible and used) and is not fully polarimetric. Like the polarimetric SFT, the many layer theory is based on the bilocal and distorted Born approximations. It also treats interference between waves reflected and transmitted through the various layer

planar interfaces coherently. The layers include air–bubbles lying around the edges of crystals. The theory is not fully polarimetric but polarization–dependent effective permittivity for a single ice crystal is used. Assumptions are made about the brine pockets, the crystal geometry and the spacing. The input consists of profiles of temperature/salinity with depth, mean tilt angle of the lag axes of brine pockets and the lengths and widths of them. The theory computes the brine volume and the effective/fluctuating permittivity.

Winebrenner et al. (1992) have used the model with 8 layers in the CRRELEX–Experiment (Cold Regions Research and Engineering Laboratory). It shows lower horizontally polarized emissivities at 10 GHz similar to the data. The predicted feature is an interference fringe caused by coherent interaction between field contributions from different layers within the ice. The model predicts mainly emissivity variations due to variations in the reflectivity of the stack of layers. The reflectivity variations are due to variations in the salinity. Neglecting the salinity profile leads to unrealistic results. Coherent effects are essential to explain the observed features. Emissivities computed from any single–layer–model oscillate as function of frequency and incidence angle more than observed. Milder sensitivity to values chosen for mean brine pocket tilt and elongation are observed. Like the polarimetric SFT the model calculates emissivities at 90 GHz too low.

2.1.4 Major gaps and recommendations

Sea ice types are defined statistically according to the WMO scheme, i.e. as statistical properties of extended regions of frozen sea surface. On the other hand, sea ice emissivity models need as input microphysical properties of completely deterministic sea ice structures. The match between both is not obvious, neither is known if there exists any. As a consequence, analyses of ice cores which give information about the ice structure in a single point do not allow to infer directly to microphysical properties of sea ice types. As long as we do not know the relation between macroscopic ice types and their microphysical structures, difficulties are to be expected when modeling the emissivity of sea ice types.

Current models calculate the emissivity of one deterministic structure as it could be produced in a laboratory experiment. But in nature, they are never found in an extent large enough to be detected with passive microwave instruments.

We recommend the **Many Layers SFT Model** to be used in the combined model because it is the only model able to

- reproduce the observed emissivity minimum near 10 GHz
- includes profiles of parameters to the ice structure.

2.2 Open–Ocean Models

2.2.1 Physical Background

The occurence of free ocean surfaces and areas of mixed ice–ocean surfaces requires the consideration of the contribution of the open water surfaces to the radiative transfer in the polar regions. Due to the low emissivity ranging from 0.4 to 0.7 (nadir view) at 10 GHz to 157 GHz, the reflectivity of the ice free surface has to be calculated separately.

It is common practice to describe the reflectivity of natural surfaces by their bistatic scattering coefficients, which include the effect of polarization. Electric fields interacting with such a surface undergo a change into a state of polarization to become horizontally or vertically polarized. The integration of the bistatic coefficients γ over the upper hemisphere leads to the reflectivity of the surface Γ with polarization P (=v (vertical), h (horizontal)), and θ and ϕ denote the zenith and azimuth angles, respectively.

$$\Gamma_P(\theta) = \frac{1}{4\pi \cos(\theta)} \int_0^{2\pi} \int_0^{\frac{\pi}{2}} \gamma_P^0(\theta, \theta_s, \phi, \phi_s) \, \sin(\theta_s) \, d\theta_s \, d\phi_s \tag{2}$$

where the scattering coefficient for the vertical reflectivity Γ_V is combined by

$$\gamma_V^0(\theta, \theta_s, \phi, \phi_s) = \gamma_{vv}^0(\theta, \theta_s, \phi, \phi_s) + \gamma_{hv}^0(\theta, \theta_s, \phi, \phi_s) \tag{3}$$

and for the horizontal reflectivity Γ_H by

$$\gamma_H^0(\theta, \theta_s, \phi, \phi_s) = \gamma_{hh}^0(\theta, \theta_s, \phi, \phi_s) + \gamma_{vh}^0(\theta, \theta_s, \phi, \phi_s) \tag{4}$$

The small penetration depth of about 1 mm at micorwave frequencies justifies the assumption that there is no transmission into the water body. Herewith the emissivity of the surface is determined by

$$e_P(\theta, \theta_s, \phi, \phi_s) \; = \; 1 \; - \; \Gamma_P(\theta, \theta_s, \phi, \phi_s) \tag{5}$$

In the case of a plane surface the bistatic coefficient γ^M can be deduced directly from the Fresnel reflection coefficients R_V and R_H.

$$\gamma_P^M(\theta) \; = \mid R_P(\theta) \mid^2 \tag{6}$$

with

$$R_V(\theta) \; = \; \frac{\epsilon_w \cos\theta - \sqrt{\epsilon_w - \sin^2\theta}}{\epsilon_w \cos\theta + \sqrt{\epsilon_w - \sin^2\theta}} \tag{7}$$

$$R_H(\theta) \; = \; \frac{\cos\theta - \sqrt{\epsilon_w - \sin^2\theta}}{\cos\theta + \sqrt{\epsilon_w - \sin^2\theta}} \tag{8}$$

where θ is the viewing zenith angle and ϵ_w the complex dielectrical constant of the water. The latter is a function of the frequency, the sea surface temperature (T_0) and, especially at frequencies below 5 GHz, also a function of salinity (Simmer 1994).

The decision to consider a surface to be flat can be made by the Fraunhofer criterium given by Ulaby et al. (1982)

$$\sigma < \frac{\lambda_{em}}{32 \cos \theta} \tag{9}$$

with σ being the standard deviation of the irregularities of the surface and λ_{em} being the electromagnetical wavelength by which the surface is detected. Non–plane surfaces lead to a more complicate structure of the interface the microwaves have to interact with. The behaviour of the scattering matrix of these surfaces differ with the increase in windspeed more and more from that of the specular case. With increasing roughness the diffusivity increases and scattering in all upper directions occur in the single scattering mode. Additionally, multiple scattering and shadowing effects have now to be taken into account.

The increase in roughness is achieved by an increase in momentum transport to the ocean surface. The wind stress roughenes the water interface expressed by its velocity dimensioned quantity the wind friction velocity u_*. This quantity is in close relation to the roughness 'seen' by the detectors than the commonly used wind speed. With u_* other contributions, which lead to a change in wind stress and therefore a change in roughness (e.g. stability), can be considered. This is important escpecially in the polar regions, where cold air outbreaks from ice or snow areas reach the open water quite frequently and lead to high instability of the marine boundary layer (refer to section 2.2.5).

The decrease in reflectivity due to an increase in roughness can be taken into account with a surface model by two different approaches:

1. The change is described by an empirical model as function of the surface parameters windspeed, T_0, salinity, view angle

2. The change is calculated based on first principles similar to (2) where the value of the scattering coefficients depends on surface roughness parameters which can be derived from wave spectra.

2.2.2 Surface Reflection Models

It is almost thirty years ago that the first promising model was suggested by Stogryn (1967), which calculates the scattering pattern as integration of the scattering coefficients weighted by the slope distribution of the surface waves. This is the base of many models often referred as *Kirchhoff*–model (one–scale model).

Further investigations led to analytical two–scale models, but they have not been established as working models due to their complexity and computational cost (Wu and Fung 1972; Wentz 1975; Fung and Eom 1981). Additionally, these models have been validated only for frequencies up to 19.35 GHz.
With this background in mind empirical formulations have been developed (Wisler and Hollinger 1977; Wentz et al. 1986; Wentz 1992). Recently attempts have been undertaken to combine these models with parametrizations to come to a higher accuracy without prolonging the computer time too much (Petty and Katsaros 1994). Alternatively, improved composite models with adequate approximations in the time consuming calculations are suggested (Guissard and Sobieski 1987; Schrader and Liu 1995).

Parametrization based on ground measurements (Wisler and Hollinger 1977) This parametrization describes the change in emissivity Δe due to wind speed without the contribution of foam. The tower based measurements were carried out near Bermuda in the western Atlantic Ocean by Hollinger (1970, 1971) with microwave radiometers at frequencies of 1.41 GHz, 8.36 GHz and 19.35 GHz over a range of wind speed from calm to 15 m/s. The parametrization needs the wind speed, frequency, incidence angle and sea surface temperature. The term Δe is then added to the emissivity of a specular surface e_0

$$e = e_0 + \Delta e \tag{10}$$

The ease of the application makes this model very popular for radiative transfer calculations (Schlüssel and Luthard, 1991; Simmer 1994). For simplicity it is used even at higher frequencies of $\nu > 19.35$ GHz, although it is not valid for this range.

Parametrization based on satellite measurements (Wentz 1992) The parametrization gives the amount of the wind–induced emissivity Δe, which includes wind *and* foam effects. It has been derived from satellite measurements of the brightness temperature by SEASAT and estimations of the windspeed from Scatterometer measurements of SEASAT, too. Both are regressed to find a relationship of the wind and the emissivity, which includes all effects apart from that of a specular surface. The angle dependency with respect to the SSM/I (Special Sensor Microwave Imager) is considerated by an additional term in the parametrization. The effective emissivity is calculated by

$$e = e_0 + \Delta e + \beta U(\theta_i - 49^o) \tag{11}$$

where e_0 is the emissivity of the specular surface and β is an angle correction factor for the incidence angle of SSM/I, U is the wind speed. The regression coefficients to determine the wind–induced emissivity Δe are adjusted to measurements of the brightness temperature by the SSM/I by a change of 10% to their original values.

Approximated two scale Model (Guissard 1987) This approach uses the *Kirchhoff*-model which regards the long gravity waves as roughness elements. These are approximated by a surface with inclined facets which are distributed Gaußian. The reflection is assumed to be specular on these facets. The small scale roughness is considerated by an approximation of the small pertubations to calculate the effective reflection coefficient of such a surface. Foam effects are not included. Their presented comparison of model simulation with the radiometric tower-based measurements of Hollinger (1971) shows no satisfactory agreement for the whole range of view angles (Guissard and Sobiesky 1987). Further problems seem to arise at their model with to long computer times (Guissard et al. 1994).

Parametrized model based on the *Kirchhoff*-model (Petty and Katsaros (1994))
This approach uses the *Kirchhoff*-model to calculate the emissvity of the ocean surface covered with long gravity waves as the large scale roughness component. Shadowing effects are ignored and multiple reflection is incorporated only up to a second reflection. The change in emissivity given as the result of the calculations over a typical range of wind speeds, sea surface temperatures, salinity and incidence angles is parametrized with respect to effective slope variance, incidence angle and sea surface temperature for each SSM/I frequency.
The parametrization in Δe is then used in radiative transfer calculations over a specified cloud free data set to calibrate these simulated brightness temperatures against SSM/I measurements which introduces another correction term to the parametrized emissivity.
All other contributions influencing the emissivity (small scale roughness, foam etc.) are considerated by another parametrization, which is derived from an analysis of SSM/I measured brightness temperatures at different wind speeds. This additional change in emissivity is incoperated over the assumed foamcoverage. This model is valid for SSM/I frequencies only.

2.2.3 Three Scale Models

A three scale model has been developed at the Institute of Marine Sciences (IFM), Kiel. It has been implemented into a microwave radiative transfer model used at the IFM. This model allows the calculation of the scattering matrix of a wind-roughened and foam-covered ocean surface.

The first scale is described by hydrodynamical waves with radius of curvature larger than the wavelength of the electromagnetic waves by which the surface is detected. These are mostly gravity waves. The formalism to calculate the scattering coefficients of such a surface is given by the *Kirchhoff*-model, assuming specular reflection on the inclined portions of the waves (facet model). The second scale is given by the short waves, which

remain in the wave spectrum if the waves of the first scale are removed. These are typically the very short gravity waves and the capillary waves depending on frequency. The scattering behaviour of this roughness scale is calculated by an approximation of the small pertubation method. This leads to a modification of the Fresnel-coefficients, which are used to calculate the reflectivity of each facet. The third scale is incorporated by the changes in reflectivity due to whitecaps and foamstreaks, which are separately considerated. This leads to a further modification of the reflection coefficients.

The first and second scales are separated by the cutoff wavenumber, which is determined in dependence of the frequency and the surface stress. It's value is choosen by the requirement that the models of the first and second scales have to be valid. A normalization in the integration procedure of the first scale leads to an exact treatment of the mathematical problem. It shortens the computer time by a factor of eight in comparison to a facet model version with high resolution to come to the same accuracy in reflectivity. The reduction in reflectivty due to shadowing effects is incorporated. The effects of multiple scattering are considered by an approach described in Guissard and Sobieski (1987). This method computes the reflectivity for an perfectly reflecting surface. This 'perfect' reflectivity is used for the correction of the single scattering reflectivity.

The model is validated qualitatively against measurements at 8.36 GHz and 19.35 GHz. A quantitative comparison could be evaluated at frequencies of 89 GHz and 157 GHz with radiometric measurements made by the UK Met Office from an aircraft at a flight altitude of 60 metres with MARSS (Microwave Airborne Radiometer Scanning System). The differences between the simulated and the measured brightness temperatures show a small underestimation by the model of 2.1 K and 5.5 K at 89 GHz and 157 GHz, respectively. However, these values are within the estimated error ranges. Thus the model has a large range of validity in frequency verified from 8.36 GHz up to 157 GHz.

The three scale model is considered for microwave radiative transfer calculations of frequencies of the actual (SSM/I, ATSR[2]) and future radiometer designs (MIMR[3], AMSU[4]).

2.2.4 Consideration of Foam

A third contribution to the change in reflectivity occurs by the appearance of foam. With its low reflectivity in the microwave regime with a typical value of $\Gamma \sim 0.1$ (Williams 1969) at 19 GHz and $\Gamma < 0.05$ at higher frequencies (Bordonskiy et al. 1978). Foam effects can contribute a considerable amount to the brightness temperature of the ocean

[2]Along Track Scanning Radiometer

[3]Multifrequency Imaging Microwave Radiometer

[4]Advanced Microwave Sounding Unit

surface. Their effective contribution depends on the fractional area within the field of view the surface is covered by foam structures. It is suggested to separate foam into those portions of white caps and streaks due to their different occurence on the surface depending on windspeed, stability, fetch, salinity and organic materials on the surface layer, and due to their different behaviour in scattering.

There are a lot of empirical models relating the foam coverage to the wind speed (Wu 1979; Monahan and O'Muircheartaigh, 1980), to the friction velocity (Monahan and O'Muircheartaigh 1986), or to the wind speed and kinematic viscosity (Monahan et al. 1990). Furthermore the models differ from each other due to the data taken into account with different wind speed and temperature ranges.

The production rate of white caps increases with the sea surface temperature. Due to a decrease of the kinematic viscosity with the temperature there is a higher probability of breaking of waves. Therefore, white caps are produced more frequently at the same wind speed over warm water than over cold. Furthermore, the thickness of the foam layer produced is an increasing linear function of the sea surface temperature (Abe 1957). On the other hand the stability of foam increase with a decrease in temperature in an exponential way (Bortkovskii 1987). In summary these effects don't cancel each other, but lead to a higher effective foam coverage in warm water regions than in cold water masses. This is represented by the different empirical models of Monahan and O'Muircheartaigh (1980, 1986), which were derived from observations over differently temperatured water masses.

The physical behaviour presented above can be found in the threshold windspeed U_B, at which the probability of the appearance of white caps exeeds 50%. A sea surface temperature $T_0 = 275$ K leads to a threshold wind speed $U_B = 3.3$ m/s and is much lower than the commonly used $U_B = 7$ m/s (Wilheit 1979). In the case of an instably stratified boundary layer with a temperature difference of $T_0 - T_{air} = 5$ K this decreases to $U_B = 1.9$ m/s (Monahan and O'Muircheartaigh 1986; Thorpe 1986).

2.2.5 Environmental Conditions

The necessity to consider the reflectivity of free–ocean surfaces in the investigation of radiative transfer over ice is caused by the appearance of mixed ice surfaces. These can be divided roughly into three types:

- small patches of water lakes as melt–water pools or the areas of open water in pancake–ice. These can be classified to have small expansion so that their water surface roughness is produced only by the local wind field. Due to its origin the melt water is free from salinity.

- Polynias and leads with small expansions, by which the ice cove exeeds the ice free portion. The roughness of these surfaces can be regarded not to be influenced by fetch or currents and therefore long waves, too. They can be assumed to be mostly plane or to be roughened by the local wind field. Their salinity is similar to that of the open ocean or less, depending on the genesis of the surrounding ice (Moss and DeLeiris 1992).
- The boundary regions of the ice covered area characterized by large polynias or drifting plates and ice mountains. In this case the roughness of the ice–free surface is described by the same characteristics as the open ocean with its dependencies on fetch, swell and currents modifying the wind stress. The latter can result in higher values than in the inner ice regions due to high instability by cold air outbreaks blowing over the warm ocean currents.

The influence of the warm North Atlantic current and the oceanic origin of the Arctic ice makes the difference in the larger ice coverage variability of the Arctic regions in comparison to the mostly continental Antarctic ice sheet.
From the climatological point of view (Atlas of the US Navy 1958) for the Arctic ocean there is a probability of 80 – 100% of closed ice coverage in February with its boundary to the open ocean to be west of 50°E (Nowaya Zemlya), south of 55°N (Spitzbergen) in the eastern part and 60°N (Baffin Island) in the North West Atlantic. In September the ice edge moves back to 80°N in the North East Atlantic and to 75°N in the other polar regions. The Labrador Sea can be expected to be ice free. But there is a high variablity in the extent from year to year.
The variable ice blanket belongs to the winter ice, which is characterized by its young age (one year or less). Its surface is strongly influenced by winds and currents which press it together or pull it apart to create polynias.

Ice mountains are found in the open ocean with a maximum of occurence in spring time. Their boundary of northward drift corresponds with 40°S latitude in the South Atlantic ocean and 50°S latitude in the Pacific ocean. In the arctic region they can be found mainly in the southern part of the Labrador Sea eastern of Newfoundland (Dietrich et al. 1975).

The wind conditions are controlled by high pressure systems over the ice covered regions leading to offshore wind directions or coast parallel winds. In February there are mostly northerly and easterly winds west of Greenland. As an average their speed does not exceed 6 m/s with a probability of 50 to 70%. Around the south coast of Greenland in only 40% of the cases the wind speed is lower than 6 m/s, but the probability for wind speeds to be higher than 14 m/s is still 20%. The wind conditions on the ice edge east of Greenland are characterized by offshore winds with 60% lower than 6 m/s. In the open water of the North Polar Sea east of 15°E all wind directions are possible, but the main

direction is the offshore component. However, the wind speed as an average is higher here than in the western parts around Greenland and there is only 30 to 40% probability of winds less than 6 m/s, but 60% of wind speeds between 7 and 14 m/s (Atlas of the US Navy 1958).
The coastal wind in the Antarctic polar regions are characterized by catabatic winds which can reach 22 m/s. Another component are the offshore winds produced by the large temperature difference between the ice and the ocean surface. In average there is a wind speed of 11 – 12 m/s at the east Antarctic coast. A third component to the Antarctic wind pattern is given by storms leading to wind speeds up to 40 m/s (Moss and DeLeiris 1992).

The wave height climatology of the regions which are expected to be ice covered up to 50% shows that the open water is never observed to be calm. On the contrary there is a probability of 20% that wave height exceeds 1.6 metres. With 60 – 80% probability one can expect a mean wave height greater than 1 metre.

The cold air masses over the ice covered regions and the offshore wind directions lead to a high instability of the marine boundary layer, where the wind starts to blow over open water. This situation can be found in winter time all around the ice boundary. The temperature difference T_{air} - T_0 is in 60% of the cases less than 10 K otherwise higher.
In summer low instability with temperature differences lower than 5 K are found with 60% probability. Otherwise there occur neutral conditions over open water near the ice edge in 10 – 20% of the cases and sometimes the stratification will be slightly stable. The antarctic temperature difference variability is slightly higher in average. The differences range from 7 to 19 K in winter time to nearly neutral conditions in summer time (Moss and DeLeiris 1992). The boundary of ice extension corresponds to the isotherm of $-1\,^{\circ}C$ with a probability of more than 50%.

The general circulation scheme of surface currents along the ice edge is determined by coast parallel currents with a strong signal of 0.5 m/s in the case of the North Atlantic current between Spitzbergen and the North Cape going northwards and the East Greenland current drifting southwards. In the eastern part of the North Polar Sea the surface currents have no preferred direction and can be considerated to be influenced mainly by the local wind field. There is a markable circumpolar current around the Antarctic with a speed of 0.15 m/s in average and easterly direction. Large eddies are found in the basins (i.e. Weddel Sea) with a west component.

2.2.6 Recommendation for Oceanic Model

The recommendation of a surface reflection model depends on the requirement in frequency validity as well as the oceanographic surface conditions it has to be used for. Today most frequent measurements of the brightness temperatures over polar regions are carried out with the SSM/I. Future planned missions with MIMR widens the range of frequencies especially to the lower channels which are more sensitive to the surface signals.
With this background in mind it is reasonable to choose a surface model with a large range of validity in frequency as the three scale model provides.

The consideration of the signal of the melt water pools and small polynias to the emissivity of the otherwise ice covered surface requires a model which takes the fetch limited roughness structures of these into account. These can be expected to be small scale waves as short gravity and capillary waves. There is no chance for the development of long gravity waves even at high winds. Only the composit models allow to distinguish between different roughness scales.
Furthermore, the frequent occurence of high instability of the boundary layer requires a model where the reflection function depends on the friction velocity and not on the wind speed only.

The foam coverage should be calculated by an empirical expression, which was derived from cold water data. The frequent occurence of non-neutral stratification conditions in the boundary layer over the open water makes the consideration of the stability effects necessary. Therefore it is recommended to calculate the foam coverage of the whitecaps by the model of Monahan and O'Muircheartaigh (1986):

$$FC_{wc} = 3.4 \times 10^{-2}\, u_*^{3.279}. \tag{12}$$

The coverage of foam streaks can be calculated by an approach of Ross and Cardone (1974), which is deduced from measurements over the Northern Atlantic and the North Sea during spring time at low water temperatures:

$$FC = (1 + R_{sw}) FC_{wc}, \tag{13}$$

where FC is the total coverage of foam structures on the water and R_{sw} is the ratio of foamstreaks to whitecaps with R_{sw} = -1.99 + 0.25 U_{20} (U_{20} is the wind speed measured in a height of 20 m).

The requirements above and the higher flexibility in frequency dependency let to the recommendation of the three scale model. Due to its efficiency this is suitable for the coupling with an ice model as surface model in total or it can be used separately.

2.3 Atmospheric Models

The simulation of the radiative transfer in an arbitrary attenuating medium requires the solution of the radiative transfer equation (RTE) describing the variation of the radiance L_ν at frequency ν within the medium along the optical depth δ_ν:

$$\cos\vartheta \frac{dL_\nu(\delta_\nu,\vartheta,\varphi)}{d\delta_\nu} = -L_\nu(\delta_\nu,\vartheta,\varphi) + (1-\omega_{0,\nu})B_\nu(T) \qquad (14)$$
$$+\frac{\omega_{0,\nu}}{4\pi}\int_0^{2\pi}\int_0^{\pi} P_\nu(\vartheta',\varphi',\vartheta,\varphi)L_\nu(\vartheta'\varphi')\sin\vartheta' d\vartheta' d\varphi'$$

where ϑ is the viewing zenith angle, φ is the azimuth angle, ϑ' and φ' are the corresponding incidence angles, ω_0 is the single scattering albedo, defined as ratio between scattering and extinction coefficient, B is Planck's function, T is temperature, P is the scattering or phase function. In the case of polarized radiation the radiance must be replaced by the Stokes vector $\mathbf{L}$ consisting of four components, that can be represented by vertically and horizontally polarized radiances and their complex correlations. For the description of the radiation field in ice, atmosphere or the coupled ice-atmosphere system equation (14) must be integrated. There are only very few special cases where this can be done analytically. Those special cases do not represent the real world and therefore, (14) must be integrated numerically using a radiative transfer model. The integral term in (14) is the main obstacle to the solution of the radiative transfer equation and gives rise to the various different approaches for its solution (Stephens 1994).

Radiative transfer models (RTM) require in principle three ingredients:

- A numerical solution of the radiative transfer equation
- A description of internal radiation sources; in the microwave spectral domain two sources are relevant, the thermal emission described by the radiation laws of Planck and Kirchhoff and the radiation source emerging from multiple scattering
- Knowledge about the cosmic background radiation as external source
- A description of the optical depth in terms of processes originating from gaseous absorption, absorption by cloud and rain particles and the scattering at cloud and rain particles

Atmospheric models that can be used for the simulation of microwave radiative transport broadly classify in two groups: Simple models only handle absorption and emission in the atmosphere and can be used as long as the optical depth of clouds or rain is small. At higher optical depths multiple scattering effects become important and must be included in the models.

Usually, radiative transfer codes are 1–dimensional, although 3–dimensional effects due to fields of broken clouds or cloud–layer discontinuities must be expected. However, the 3–dimensional models that are currently being developed do not have the maturity to be included in the current study since they are restricted to simulations of radiative transfer in idealized situations that do not occur in nature.

Horizontal inhomogeneities must be included in radiative transfer calculations. In the case of nadir-viewing geometry this can be handled by multiple calculations for homogeneous cases with subsequent weighted averaging. For limb radiative transfer the horizontal inhomogeneities must be included directly in the radiative transfer model (Hollweg et al. 1995b). The assumption of a plane parallel atmosphere is adequate to describe the spherically layered atmosphere if atmospheric layers are thin enough (i.e. ≈ 1 km) and if the zenith angle instead of nadir or scan angle is considered. Necessary features of a model to be coupled as a module into an ice–atmosphere model are:

- Acceptance of arbitrary input profiles of atmospheric state parameters
- Both, upward and downward radiative transfer can be calculated
- Radiances or brightness temperatures as upper (space radiance) and lower (surface reflectance and emittance) boundaries can be incorporated
- Inclusion of a cloud and precipitation model accounting for particle size distribution, particle shape, and orientation or acceptance of pre-calculated phase functions, attenuation coefficients and single scattering albedoes

The simulation of the radiative transfer is usually handled monochromatically even for broad spectral responses of the space–borne radiometers. In view of the narrow spectral response of radiometers operated at microwave frequencies the calculation of broad–band transmittances is usually avoided; instead, line–by–line calculations are carried out before convolving the radiances with the spectral filter of the instrument.

2.3.1 Solutions of the Radiative Transfer Equation

The formal solution of the radiative transfer equation is a purely mathematical task and does not require any knowledge about the physical properties like attenuation coefficient, phase function, single scattering albedo, internal and external sources. But, the modelling of the atmospheric radiative transfer requires the inclusion of the of the physical parameters. Hollweg et al. (1995a) have reviewed the RTE solutions in detail. The major findings are repeated here for completeness and are related to the current investigation.

2.3.1.1 Spherical Hamonics Method (SHM)

In this method the phase function is expressed as series of Legendre polynomials and the radiance is expanded into spherical harmonics. Multiplication of the RTE with the complex conjugate of the spherical harmonics and integration over the solid angle splits the RTE into a system of differential equations which can be solved after specification of the boundary conditions. Recent developments have been described by Takeuchi (1988) and Evans (1993).

Advantage: The SHM delivers radiances at any viewing angle.

Disadvantage: Many series terms are necessary if the phase function is strongly peaked (i. e. in the Lorenz-Mie scattering domain) leading to expensive computations.

2.3.1.2 F_N Method (FN)

This technique is very similar to the SHM but includes a different decomposition of the phase function (Devaux and Sievert 1980). A fully polarized version without internal sources has been described by Garcia and Sievert (1989).

Advantage: The method is more accurate than SHM and computationally efficient.

Disadvantage: The technique is conceptually more complicated than SHM and more difficult to implement numerically.

2.3.1.3 Discrete Ordinates Method (DOM)

The DOM is based on a Fourier decomposition of the RTE where the zenith angle is discretized according to the double-Gauß quadrature. The vertically inhomogeneous atmosphere is subdivided into a set of homogeneous layers where the RTE is formulated in matrix form separating upward and downward directions. This leads to a system of coupled ordinary differential equations with constant coefficients which can be solved by finding eigenvalues and -vectors numerically. Kobayashi (1991) and Gabriel et al. (1993) have described three dimensional approaches of the DOM. A review of multiple scattering with emphasis on the DOM is given by Stamnes (1986). A Fortran code, named DISORT, has been developed and validated by Stamnes et al. (1988) and Tsay and Stamnes (1990). A coupling of DOM with the adding method has been proposed by Nakajima and Tanaka (1986).

Advantage: The solution and the computing time required does not depend on the optical depth of the atmosphere; the method supplies transmission and reflection of each layer; the solution is numerically stable.

Disadvantage: Sharply peaked or strongly varying phase functions might require higher orders of discretization.

2.3.1.4 Adding, Doubling, and Matrix Operator Method (MOM)

Instead of the numerical modelling of the RTE an equivalent approach, the interaction principle, is used. After discretization of the ordinates radiances are transformed to vectors and reflection and transmission functions into matrices. The azimuthal dependence is described by decomposition of the radiation field in a Fourier series and by developing the scattering phase matrix in a series of Legendre functions. Formulation of the interaction principle for infinitesimal layers, doubling until the optical depth of a thick homogeneous layer is reached and subsequent adding to other homogeneous layers allows the description of the full multiple scattering problem including polarization in a vertically inhomogeneous atmosphere. An azimuthally dependent approach including polarization has been described by De Haan et al. (1987). Two different approaches are used to compute the Fourier coefficients of the phase matrix: The usual integration method including the scattering matrix by rotating from the reference plane into the scattering plane and back into the reference plane, and the expansion method (Kuščer and Ribarič 1959) where the Fourier coefficients are expressed in the expansion coefficients of the scattering matrix using generalized spherical functions (Siewert 1981). The latter is also used by Deuzé et al. (1989) and Mishchenko (1990). Generally, the expansion method is faster by a factor 1 to 5 in order to gain the same accuracy. Recent publications related to the use of MOM in microwave radiative transfer considering the full Stokes vector have been given by Evans and Stephens (1991), and Bauer and Schlüssel (1993).

Advantage: The MOM uses simple mathematical operations which lead to an easy physical interpretation; the reflection and transmission operators are obtained for all incident and emergent angles at once and include all orders of scattering; the MOM is not retstricted to any size of the optical depth; the resulting reflection and transmission operators can be coupled to arbitrary modules describing surfaces and/or attaches systems like ocean or sea ice.

Disadvantage: Not known.

2.3.1.5 Finite Difference Method (FDM)

The RTE is expanded into a Fourier series. As vertical coordinate the altitude is chosen, the zenith angle is discretized and the scattering integral is approximated by a Gaussian quadrature. The set of differential equations are approximated by finite difference equations which can be solved. The FDM has been used in one and two dimensional radiative transfer problems by Gerstl and Zardecki (1985). For the calculation of visible and near UV radiative transport the FDM found another realization in the GOMETRAN model (ESA 1993).

Advantage: The FDM is computationally fast, can handle large optical depths and is flexible with respect to number of grid points on altitude and zenith angle coordinates.

Disadvantage: The selection of grid points in vertically inhomogeneous atmospheres and for anisotropic phase functions critically depends on the actual case to be simulated. Numerical instabilities arise when the difference between upward and downward radiances becomes smaller than about 10^{-4}.

2.3.1.6 Gauß Seidel Iteration (GSI)

The RTE is solved formally, the vertical coordinate and the solid angle are discretized in equal parts of the optical depth and solid angle increments, repectively. After quadrature of the source function integral with respect to the solid angle the resulting linear equation system is solved iteratively with the Gauß-Seidel method. Koepke and Kriebel (1978) made use of the GSI to calculate the solar radiation field including polarization in an azimuthally dependent atmosphere model including an anisotropically scattering land surface. The multiple scattering is handled according to GSI in the LOWTRAN7 and FASCOD3 codes which are commercially distributed but not described in literature.

Advantage: The GSI does not require series truncation.

Disadvantage: The computational effort increases linearly with the optical depth and is not recommended for calculations with $\delta \gg 1$.

2.3.1.7 Successive Order of Scattering (SOS)

The SOS method calculates the radiances individually for photons that are scattered once, twice, three times and so on with the total signal obtained as the sum over all orders. Deuzé et al. (1989) successfully used the SOS technique for the description of the azimuthally dependent fully polarized radiation field in a coupled ocean-atmosphere system.

Advantage: The SOS method is transparent with respect to the physical meaning of single orders of scattering; the radiances are computed for all zenith angles and vertical heights defined by the corresponding quadratures at the same time.

Disadvantage: Multiple scattering processes are solved order by order, SOS is therefore slowly converging for high optical depths and single scattering albedoes approaching unity. In the case of conservative isotropic scattering the 50th order scattering can still contribute about 1% to the total reflection function (Goody and Yung 1989). However, the use of asymptotic expressions for the approximation of higher order scattering can accelerate the computations.

2.3.1.8 Two-Stream Equations (TSE)

Integrating the radiative transfer equation independently over both hemispheres leads to a set of coupled, first-order differential equations which are known as TSE. Usually, the TSE are employed for flux density calculations in atmsopheric energy-budget studies.

However, they have been used in radiative transfer calculations for the use with remote-sensing applications, too (Doerffer 1980; Schiller and Doerffer 1993).

Advantage: The method can be solved analytically and is computationally fast.

Disadvantage: TSE calculations are designed to give radiative flux densities, not radiances and are therefore to be considered as inaccurate with respect to forward calculations in the field of remote sensing.

2.3.1.9 Monte Carlo Method (MCM)

The MCM is the most general method. It considers absorption and scattering of photons as a stochastic process where the phase is regarded as a probability density function for the redistribution of photons in different directions. Therefore it can handle the radiative transfer in media with arbitrary geometrical configurations (Goody and Yung 1989). Recently, O'Brien (1992) proposed an accelerated MCM by selecting photon trajectories to sample the integration domain optimally and by estimating the rate of decay in the multiple scattering series. It was found that this quasi Monte Carlo method (QMC) is both robust and applicable with any scattering geometry.

Advantage: Easy handling of three dimensional transport or particle geometry is possible; a large number of layers can be specified without increasing computing time; calculation of the polarized radiation field requires only twice as much time as for the radiance field.

Disadvantage: Statistical fluctuations in the results can reach several percent when computer time is restricted to tolerant amounts; the MCM is impracticable for extremely large optical depths. An improvement of the MCM has been achieved by the QMC which partly abolish these disadvantages.

2.3.1.10 Emission Absorption Model (EAR)

In cases where the single scattering albedo is small the scattering can be neglected and only emission and absorption (as well as surface reflection) must be included in the radiative transport. Comparisons with complete model runs show that the EAR models can be utilized in infrared and microwave radiative transport calculations simulating space–borne radiometric measurements (Schlüssel and Emery 1990).

Advantage: Easy and fast computation of microwave radiative transfer; inclusion of first two components of the Stokes vector without increase of computing time.

Disadvantage: No inclusion of scattering processes; no indication where scattering becomes important.

2.3.2 Accuracy of Models

The model accuracy was analysed by Lenoble (1985). The models SHM, DOM, SOS, FN, and MOM produce radiances emerging from cloudy or hazy atmospheres with accuracies better than 1%. The SHM technique shows problems when sharp forward peaks in the phase functions occur because of truncation after too few terms. Mengüç and Iyer (1988) report an 1.3% agreement between SHM and FN techniques. The accuracy of MCM techniques critically depends on the smoothing of statistical fluctuations; the latter decrease with the square root of the number of photons used in the calculations. Hence, enormous amounts of computer time may be required to obtain results of modest accuracy (Goody and Yung 1989). The computational accuracy reported for the GSI is 1% (Eschelbach, 1971). The accuracy of TSE calculations is of the order of 10%; more accuracy is achieved with higher order approximations like the four or six stream models that are currently under study (Schulz 1995, personal communication). Finally, it should be stressed that limited knowledge about the fundamental physical parameters like extinction coefficients, single scattering albedoes and phase functions often introduce greater uncertainties in the radiative transfer calculations than the numerical models involved (Goody and Yung 1989).

2.3.3 Three Dimensional Transport

The one dimensional approach is not adequate to describe the radiative transfer when finite clouds are present, i.e. in cases with fields of broken clouds or at discontinuities like cloud edges adjacent to cloud-free regions(Gabriel et al. 1993). The same refers to convective rain cells which are three-dimensional objects per se. The modelling of the three dimensional radiative transfer is a complicated task because of the coupled spatial and angular properties in the Fourier decomposition of the RTE. Furthermore, for strongly forward peaked phase functions one has to include a large number of quadrature terms resolving the zenith angle. The same refers to the resolution of the azimuth angle.

2.3.4 Molecular Absorption

At microwave frequencies the atmospheric absorption spectrum is characterized by absorption due to magnetic dipole rotational transitions of molecular oxygen near 60 and 118 GHz and due to electric dipole transitions of water vapour extending from 22 GHz to the sub-millimetre domain. Nonresonant refractivity of the dry air add a small contribution to the absorption at high pressures in the lower atmosphere due to the Debye spectrum of oxygen below 10 GHz and pressure-induced nitrogen absorption above 100 GHz (Liebe 1985, 1989; Mingelgrin 1974; Stankevich 1974). A contribution of distant strong lines probably adds to the water-vapour continuum absorption in the windows between the lines. The molecular absorption to be included in the radiative transfer calculations are characterized by molecular absorption coefficients $k_\nu(p, T)$, where ν is the frequencey, p

is the atmospheric pressure and T is temperature. The knowledge about the absorption coefficients stems from laboratory measurements of spectroscopic parameters like line positions, intensities, widths, continuum absorption coefficients etc. and from calculations based on distinct models which describe absorption coefficients in terms of the line and continuum parameters and atmospheric state parameters:

$$k_\nu(p,T) = S(T)f(\nu,\nu_0,e,p,T) \tag{15}$$

where $S(T)$ is the line intensity, f is the line shape, ν_0 is the line centre and e is the partial pressure of the absorbing gas. In the lower atmosphere the shape function f is usually the Voigt function that describes the line broadening by collisional and Doppler effects. For the microwave radiative transfer related to ice–atmosphere interactions the problem can be retricted to tropospheric levels where the Doppler broadening can be ignored and only the collisional broadening according to the Lorentz line shape must be considered:

$$f(\nu-\nu_0) = \frac{\alpha}{\pi[(\nu-\nu_0)^2+\alpha^2]} \tag{16}$$

where α is the line half width. At microwave frequencies the Lorentz line shape must include a correction making the collisional processes consistent with Boltzmann statistics (Goody and Yung 1989). The correct line shape, nown as van Vleck-Weisskopf line shape (Vleck and Weisskopf 1945) reads:

$$f(\nu-\nu_0) = \frac{1}{\pi}(\frac{\nu}{\nu_0})^2\alpha[\frac{1}{((\nu-\nu_0)^2+\alpha^2} + \frac{1}{(\nu+\nu_0)^2+\alpha^2}] \tag{17}$$

which reduces to the Lorentz profile for $(\nu-\nu_0) << \nu_0$. At altitudes above about 50 km the Doppler effect has to be included and above levels of 100 km the Zeeman splitting of absorption lines becomes important (Liebe 1981; Rosenkranz 1988).

Several models describing the absorption at millimetre wavelengths can be identified in the literature. The most widely used ones are those described by Liebe and co-workers which is continuously updated with new spectroscopic information (Liebe 1981, 1985, 1989; Liebe and Hufford 1989; Liebe et al. 1991a, 1991b; Liebe et al. 1992). Other absorption models have been described by Ulaby et al. (1981) that is closely based on that of Waters (1976), by Clough et al. (1983), Edwards (1988), and Barret and Chung (1962). Besides these models including absorption line parameters together with model functions of the absorption lines and their dependencies on temperature, pressure and absorbing mass there are single line parameters tabulated in catalogues like the HITRAN 92 and 96 databases (Rothman et al. 1992). All of the models are of empirical or semi–empirical nature. The spectroscopic measurements elucidated weaknesses of the line shape according to (17) in underestimating the absorption in the windows between the absorption lines (Danese and Partridge 1989; Llewellyn–Jones 1980; Rosenkranz 1975) which led to line overlap corrections (Rosenkranz 1975, 1988) and to the formulation of absorption continua (Liebe 1981,

1985). However, the physical cause of the continua is still under debate as it is the case in the infrared spectrum. Recent atempts focus on the modification of line shapes and integration of line wings of distant lines to explain the excess absorption in the window regions (Ma and Tipping 1990). The different absorption models mentioned above include different line shapes and absorption continua.

Oxygen and water-vapour lines up to 1 THz have been described in the Liebe model assuming van Vleck–Weisskopf line shapes with overlap corrections according to Rosenkranz (1975, 1988). Dry air and water–vapour continua are added where the absorption coefficients are based on laboratory measurements. A strong negative temperature dependence is included. A concurring model for the spectrum below 300 GHz is included based on a smaller database with fewer absorption lines and a modified continuum in order to enhance the computational effort in the transmittance calculations. A different line shape model according to Gross (1955) and Zhevakin and Naumov (1963) has been included in the model of Waters (1976) that builds the basis for the model of Ulaby et al. (1981). Below 100 GHz an empirical correction is added to the contribution of the 22.235 GHz line. In the spectral range between 100 and 300 GHz the absorption coefficient consists of the sum of ten lowest frequency lines and a correction given by Gaut and Reifenstein (1971). The model by Barret and Chung (1962) uses a van-Vleck-Weisskopf line shape for the 22.235 GHz line and a continuum fitted to measurements by Becker and Autler (1946). The model of Clough et al. (1983) uses a van-Vleck-Huber line shape which reduces to the shape (17) in the microwave region. The continuum used by Clough et al. (1983) is a summation of all line contributions from beyond 25 cm^{-1} of all line centres; the continuum has been adjusted to measurements of Burch (1981).

English et al. (1994) have intercompared the four different absorption models at 89 and 157 GHz. They found a similar water–vapour transmittance for the models of Liebe (1989) and Ulaby et al. (1981) in middle latitudes whereas the model of Barret and Chung (1962) gives stronger absorption in all cases analysed. In tropical situations the model of Ulaby et al. (1981) gives less absorption than that of Liebe (1989). The model of Clough et al. (1983) agrees coarsely with those of Liebe (1989) and Ulaby et al. (1981) at middle latitudes but is in close agreement with Liebe's (1989) model for high water–vapour columns. The temperature dependence of Liebe's (1989) model is more pronounced than in the other three models, the latter show a similar behaviour with respect to the temperature.

The line coupling plays a crucial role in the absorption models, especially in the oxygen lines near 60 GHz. The model of Rosenkranz (1975) substantially reduces the absorption in the wings of the oxygen band between 50 and 60 GHz. Neglecting water vapour, this line coupling increases the surface to space transmission from 80% to 95% at 89 GHz.

Therefore, this feature plays an important role in the radiative transfer through polar atmospheres which are considered here. At 157 GHz the transmission is increased from 95% to 99% when including the line overlap correction. The model of Rosenkranz (1975) does not obey the sum rules given by quantum mechanics (Strow and Reuter 1988) when calculating the line coupling coefficients. The new models described by Rosenkranz (1988) and Liebe et al. (1992) obeys the sum rules and are therefore built on a more adequate theoretical basis than the previous approach. As a result of the sum rule the oxygen absorption should approach a constant value at high frequencies (English et al. 1994). Comparisons of model calculations with radiances at 89 and 157 GHz observed during field campaigns have been carried out by English et al. (1994). As result they found that the model of Liebe (1989) shows the best overall agreement but suffers from too low absorption coefficients in situations with high water-vapour contents. The model of Clough et al. (1983) shows similar performance results while the model of Barret and Chung (1962) shows greater deviations in middle latitudes and arctic situations. The model described by Ulaby et al. (1981) is inferior to Liebe's (1989) model in tropical cases. The observed temperature dependencies of the water-vapour continuum absorption as described by Liebe (1989) is supported by the observations. However, the best fit of the airborne measurements by the absorption spectra requires a 5% increase of the self-broadened line strengths.

The Liebe model versions as of 1981, 1989, and 1991 as well as the model of Waters (1976) have been tested in the frame of the Intercomparison of Transmittance and Radiance Algorithms (ITRA) by comparing calculated downward radiances for radiosoundings colocated with ground-based radiometric measurements at 20.6, 31.6, and 90 GHz. The match-ups consist of 110 different profiles (Westwater et al. 1990; Phalippou, 1993). The results show that the Liebe (1981) model version has the best performance with respect to bias and rms errors. At 20.6 and 31.6 GHz the model by Waters (1976) shows an excellent performance as well but is inferior at 90 GHz. The errors of Liebe's models are generally less than 2.4 K while the bias shows a maximum of 1.33 K at 20.6 GHz. The Waters' (1976) model shows good results at low frequencies but fails to show adequate ones at the higher frequency.

2.3.5 Attenuation by Clouds and Precipitation

The extinction by clouds and precipitation is handled in different ways. The full account for multiple scattering at spherical particles requires the utilization of Lorenz–Mie theory which in turn requires knowledge about the the complex index of refraction and the particle size distribution. The result from Mie calculations is a set of absorption and attenuation coefficients as well as a scattering phase matrix. Such an approach will be adequate in cloudy atmospheres and in rain situations (e.g. Evans and Stephens 1991; Bauer and Schlüssel 1993). Often, the scattering is approximated by the Rayleigh theory,

but, for large rain drops this approach is no longer justified and calculations according to the Lorenz–Mie theory should be preferred (Bauer and Schlüssel 1993). In cases where multiple scattering can be neglected (i.e. situations with small single scattering albedo) the extinction by liquid water can be approximated by pure absorption assuming a hydrosol absorption continuum that has to be included in the radiative transfer calculations. The liquid-water continuum at microwave frequencies has been described by Liebe (1981, 1985, 1989), Altshuler (1984), Liebe et al. (1989), and Lhermitte (1990). The transition from the non–scattering to the scattering domain strongly depends on the liquid and ice water densities and on the frequency.

The complex index of refraction can be computed from the complex permittivity that is given by the Debye relaxation

$$\epsilon = \epsilon_\infty + \frac{\epsilon_S - \epsilon_\infty}{1 + 2i\pi\nu\tau} \tag{18}$$

where ϵ_S is the static permittivity, ϵ_∞ is the high frequency permittivity, τ is the relaxation time, and $i = \sqrt{-1}$. Different interpretations of the Debye formula can be found in the literature describing the permittivity of liquid water and ice (e.g. Ray 1972; Chang and Wilheit 1979; Liebe et al. 1989). Different temperature dependencies of τ and ϵ_S and different experimental results lead to different values of the index of refraction at microwave frequencies (Saxon and Lane 1952; Klein and Swift 1977; Liebe et al. 1989) which are still not consolidated. A review about the optical constants of ice including the microwave region has been compiled by Warren (1984). The refractive index of snow as a mixture of ice, liquid water and air has been described by Sadiku (1985).

The scattering at non–spherical ice particles like crystals and snow flakes becomes increasinly important with increasing frequency and must be considered beyond approximately 80 GHz (Stephens 1994). Non–spherical particles have only recently been included in polarized microwave radiative transfer models. However, the corresponding models are still premature and fail to fully describe the radiative transfer in ice clouds and snow storms. The radiative properties not only depend on the refractive index and particle size distribution but also on the orientation of the particles. Early attempts swith arbitrarily oriented ice cylinders have been described by Liou (1972). Scattering at non–spherical Chebychev particles has been computed by Mugnai and Wiscombe (1986) by using the Extended Boundary Condition Method (EBCM), as formulated by Barber and Yeh (1975). Evans and Vivekanadan (1990) utilized the discrete dipole approximation, also named digitized Green's function, (Purcell and Pennypacker 1973; Draine 1988; Flateau et al. 1990) for the description of the electromagnetic scattering properties of idealized ice clouds. This method has been tested against analytical solutions (Goodman et al. 1991). In view of the computational constraints this method is suited for the study of particle scattering at microwave freuencies where small size parameters ($\ll 5$) can be expected

(Evans and Vivekanadan, 1990; Dungey and Bohren, 1992). Goedecke and O'Brien (1988) and O'Brien and Goedecke (1988) promote the digitized Green's function method for the calculation of scattering by snow crystals and other equivalent homogeneous symmetric particles. They show that the snow crystals (still of idealized shape) can be reasonably well approximated by equivalent homogeneous particles (e.g. oblate spheroids) of which mass distributions are similar to those of the snow crystals. Hence, the EBCM could be used after this approximation for an easy determination of scattering cross sections and single scattering albedoes.

Recently, Tang and Aydin (1995) have studied the polarimetric scattering from ice crystals at millimetre wave frequencies using the finite difference time domain method (FDTD) which is designed for electromagnetic scattering computations for complex shaped three dimensional particles (Kunz and Luebbers 1993). For large horizontally aligned ice crystals they found pronounced variations in dual frequency ratios (94 versus 220 GHz) and linear depolarization ratios depending on the actual shape of the crystals. They show that the radiative transfer also depends on the orientation of the ice particles for hexagonal columns, hexagonal plates, and stellar crystals.

2.3.6 Cosmic Background Radiation

In microwave radiative transfer it is necessary to include the cosmic background radiation to the downwelling radiative transfer. The cosmic background temperature defined by an inversion of Planck's function is 2.735 K as found from measurements of the COsmic Background Explorer (COBE). The COBE measurements did not show any deviations from the perfect blackbody spectrum (Schwarzschild 1990).

2.3.7 Recommendation for Atmospheric Model

From the foregoing discussions the choice for an atmospheric model merely depends on the physical ingredients like molecular absorption properties and on the adequate description of attenuation by clouds and precipitation rather than on the numerical solution of the radiative transfer equation. Candidates for the latter are the matrix–operator–method, the discrete ordinate method, and the successive order of scattering technique. The description of the molecular absorption is most advanced in the recent model by Liebe et al. (1992) including an updated model for line-overlap effects. No other description has been published in recent literature. The classical description of non-spherical cloud particles and hydrometeors in terms of Rayleigh or Lorenz-Mie theories should be replaced by a more realistic model that is capable to handle arbitrarily shaped particels. However, such models are currently under development and are not yet mature enough for an inclusion at this time. Further development and consolidation of such models seems to be indicated.

2.3.8 Review of Environmental Conditions

The environmental conditions in polar regions are extreme with respect to their temporal and spatial variation. Especially in the Arctic the surface optical properties change more dramatically during the annual cycle than in other regions (Zak et al. 1995). The annual migration of the circumpolar throughs causes a pronounced variation of the cyclonic activity and thus a great seasonal fluctuation in precipitation events. The type of precipitation also shows a strong variation depending on season and location. Deep convection with heavy snow, graupel or rain showers in the marginal ice zone can be expected in winter while stratiform clouds with weak precipitation snow, snow grains, ice pellets and star–like snow crystals prevail in the inner Arctic and Antarctic areas throughout the year. The annual amount of precipitation in the central Arctic is less than 150 mm but increases to values greater than 500 mm in western Greenland (Martyn 1992).

The monthly mean cloud cover in the Arctic varies between about 0.5 from December to March and about 0.8 in August and September (Parkinson and Washington 1979). The large–scale variation ranges from about 0.35 to 0.95. Summer fog can be expected on more than 100 days per year in the Arctic ocean. The surface temperature of the Arctic winter shows minimum values of as low as -50 °C in the centre and average values of -6 °C at the coasts of the Greenland Sea. In summer when the temperatures are controlled by the inflow of solar energy and the influence of land the temperature can rise as high as 10 °C in July (Martyn 1992). The daily temperature variation in the Arctic can be as high as 4 to 8 °C. The relative humidity in the Arctic is high with maximum values near 94% at the coasts of Alaska and Canada from May to September and up to 89% near Scandinavia in summer and 95% in the Norwegian and Barents Seas in summer.

Unlike the Arctic Antarctica is characterized by extremely low air humidity of which annual mean does not exceed 85% at the northern end of the Antarctic Penninsula and is well below 70% at the east coast. Cold air outbreaks from the inner Antarctica with humidity extremes as low as 20% are not uncommon over the sea ice areas around Antarctica. The corresponding specific humidities are less than 1 g/kg (van Rooy 1957). The cloud cover is low and clear skies can be expected from May to July where the mean cloud cover varies between 70 and 16% (Martyn 1992). The spatial variation of monthly mean surface temperatures is great. At coastal stations like the Georg–von–Neumayer–Station the average temperature is -4 °C in January and -26 °C in August. But, the entire range of temperatures varies between about 5 °C and -40 °C (Wyputta 1994).

Upper air temperatures vary from surface temperatures down to about -75 °C at the winterly tropopause over the Antarctic coast. Therefore the most cloud and hydrometeoric particles can be expected to be in the ice phase in the south polar regions. But, in the north polar summer atmosphere liquid cloud and rain drops are frequent.

2.3.9 Identified Gaps and Recommendations

The literature review has elucidated the following gaps related to the radiative transfer in microwave regions and immediately lead to recommendations for further research.

- The origin of the absorption continua in the microwave region is still unclear and its accurate quantification as well as its temperature dependence requires laboratory and field investigations.

2.4 Surface-Atmosphere Interactions

The interaction between ice and atmosphere can be divided in two different categories. The first is the atmospheric impact on the ice microphysics which in turn affect the radiative properties of the ice while the second interaction is purely radiative and determines the way how information about the ice is carried by the atmospheric radiation field to space borne radiometers.

2.4.1 Atmospheric Impact on the Ice Microphysics

The ice-atmosphere interaction is mainly driven by the annual cycle broadly determining the formation and melting of sea ice. An important influence on the annual cycle comes from the land-sea distribution which is different in both polar regions. While the Antarctic continent mainly lies south of 70° S the Arctic Ocean is a basin surrounded by continents. The Arctic ice extent therefore undergoes weaker seasonal changes than the Antarctic sea-ice belt resulting in lacking multi–year ice in the Antarctic and smaller seasonal changes in the Arctic. The evolution of sea ice according to environmental influences from open water to first–year ice is shown in figure 1 according to Weeks (1976). It clearly demonstrates the atmospheric impact by cooling and precipitation in determining the type of new ice that forms during freeze-up. Livingstone et al. (1987) broadly subdivide the sea–ice year in five seasons: Winter, initial warming (early melt), melt onset, advanced melt, and freeze–up, defined by the environmental parameters surface wetness, ice melt, snow cover, new–ice growth, and ice–surface temperature. However, the actual microphysical properties of the ice can be strongly modified by individual meteorological situations. The following subsections classify the meteorological impact by atmospheric parameters involved in the distinct interactions.

2.4.1.1 Temperature and Solar Radiation The annual cycle of air temperature and insolation determine the growth and decay of sea ice as well as the internal modification of the ice structure. The characteristic of an ice sheet is controlled by its temperature and is therefore driven by air temperature and absorbed solar radiation. However, thin sea ice drastically changes the albedo of the ocean surface during the transition from liquid

water to thin ice and therefore significantly affects the radiation budget at the sea surface (Beaven et al. 1994) resulting in a feedback of the ice on the energy exchange at the surface. A feedback on the air temperature is caused by polynyas and leads where increased turbulent exchange between ocean and atmosphere can lead to substantial changes of atmospheric temperature. Modelled results indicate a possible temperature rise up to 3 K over polynyas and leads which can in turn affect the surrounding sea–ice areas (Katcov et al. 1993). The air temperature and sea-ice temperature variations are strongly correlated but with a phase lag of about one month (Xie et al. 1994). Shokr and Barber (1994) found from field observations during the melt season that the variation of air temperature is replicated by the ice temperature but not in the salinity or dielectric properties. The ice types analysed were first and multi–year ice in the Resolute Passage (Eastern Arctic). Ono and Krass (1993) show by theoretical analyses that the penetration of air–temperature oscillations into the snow-covered sea ice increases remarkably with increasing snow density.

The brine inclusion process is temperature dependent in that the spacing of the crystal plates is almost entirely determined by the growth rate. More rapid freezing causes narrower spacing of the platelets effecting an enhanced brine inclusion which in turn leads to higher salinity (Weeks and Ackley 1986). Any change in ice temperature will be accompanied by changes in brine-pocket size resulting from freezing and melting on the walls of the pockets until the salinity of the pocket reaches a new equilibrium composition. High salinities (if not highest) can therefore be found at the top of an ice layer (Tucker et al. 1992). Brine drainage begins immediately after ice formation, occurs slowly during growth season and increases considerably during melt season. Enhanced surface melting combined with increased interconnectivity of brine inclusions almost completely removes the salt from the upper salt layers leaving air inclusions. The crystal texture within the upper metre of the ice is strongly modified by extended warming leading to rounding of crystal boundaries and decay of brine platelet structures (Tucker et al. 1992). Desalination of sea ice mainly occurs in the summer season when increasing temperatures lead to melting of ice resulting in lower equilibrium salinities in the brines. At the same time the increased brine volume likely leads to a coalescence of the brine pockets into vertical channels that effect gravity drainage of the brines and desalination (Martin 1979). The summer melt cycle also affects the crystalline structure of the ice in rounding originally sharp crystal boundaries and smearing or even eliminating the well–defined platelet structure (Gow et al. 1987).

The temperature dependence of the dielectric constant of sea ice strongly varies with the ice type. While for the relatively salt–free multi–year ice the dielectric constant does not show remarkable temperature dependencies the dielectric constant of first–year ice

increases with increasing temperature above -10 °C (Onstott 1992).

Crane and Anderson (1994) show from observations in the Kara Sea and theoretical modelling of the surface radiation balance that under clear sky conditions with increased solar input during spring and early summer melt signatures occur already below freezing temperatures. This is supported also by theoretical analyses performed by Ono and Krass (1993) and Maslanik and Silcox (1993). The freeze–thaw cycling during several days establishes a surface hoar layer with an increased penetration and absorption of solar radiation just below the surface layer. From energy budget studies in the fast–ice of the Davies Strait Barry et al. (1978) found that the air temperature is the important factor for melt processes as long as the snow cover is cooler than 0 °C. Then net radiation flux and advection of heat strongly determine the melting.

2.4.1.2 Ocean–Air Heat Transfer The initial ice formation takes place at the surface and therefore requires great heat loss at the surface while further ice formation can also occur in the water body at the lower ice boundary. As soon as a thin ice cover has been established it isolates the underlying ocean from the cold atmosphere, thus, further heat exchange is drastically reduced. Field observations and model results indicate that the most effective sea–ice formation occurs in open water areas (Roth 1994). Under cold conditions ice growth in leads occurs rapidly leading to a high bulk salinity. The surface characteristics are dominated by thin, highly saline surface skin and often formation of frost flowers. Within few hours of growth the initially smooth surface develops small–scale roughness (Perovich and Richter-Menge 1994).

The large heat fluxes from the ocean to the surface (i.e. warming of the ice from below) leads to an efficient melting of relatively thin first-year ice surrounding Antarctica. Strong turbulent surface-air heat exchange that is dominated by low air temperatures in the Antarctic sea-ice regions prevents the sea ice from surface melting (Andreas and Ackley 1982). This results in an absence of surface melt ponds and melt-pond-hummock reliefs which are characteristic for Arctic ice floes. Antarctic sea ice rarely lives longer than one or two years (Gow and Tucker 1990) resulting in the major difference between Arctic and Antarctic sea ice.

2.4.1.3 Wind Both wind and ocean waves influence the initial configuration of the solids that form during the onset of sea ice as well as the further development of sea ice. The transition from grease ice, slush and shuga to ice rind, dark or light nilas critically depends on the wind speed. Ice rind, a hard shiny crust of ice, only forms on a quiet surface by direct freezing or from grease ice while nilas can easily be bent on wind waves

or swell and therefore allow for slightly higher wind speeds (WMO 1989). Major wind-induced differences in crystal structures can be found between Arctic and Antarctic sea ice. In the Antarctic more frazil ice forms than in the Arctic resulting also in higher frazil-rich pancake ice and ice sheets in the Antarctic sea ice (Tucker et al. 1992). Platelet ice consisting of large plate- and wafer-like crystals have been observed only in the Antarctica so far (Lange et al. 1989).

In leads the new ice can accumulate under the action of wind producing thick (up to 1 m) new-ice layers at the lee side of the lead or polynya. Wind-driven circulations like the Langmuir circulation can cause an alignment of new ice in bands parallel to the wind direction similar as wind rows where sea weed is accumulated at the surface (Tucker et al. 1992).

Pressure ridges are formed by ice movement that is driven by wind and currents. Ridges and hummocks are weathered and rounded by the influence of winds modifying the block structure to an extent that leaves no evidence of the original shape. Compacted and hardened snow drifts, known as sastrugi, taper away in the direction of the wind. They can reach lengths of several hundred metres and heights of the order of one metre. The small-scale sea-ice roughness can also be the result of wind-driven ice movement and the wind-induced surface erosion as well as the redistribution of snow and is continuously under modification (Tucker et al. 1992).

Severe storms can open the ice cover producing polynyas with low ice concentration as observed in the Tatarskiy Strait (Martin et al. 1992) as well as in the Alaskan, Siberian, and Canadian coastal polynyas (Cavalieri 1994). Subsequent refreezing with thin ice is observed shortly after the storm events.

Recent studies of Rikiishi and Takahashi (1993) show that the evolution of sea ice and the variation of sea ice cover also strongly depends on the wind direction and fetch of the wind. However, those processes are under investigation and do not allow any conclusions yet.

2.4.1.4 Precipitation The main cause of snowfall over sea ice is the resulting snow cover which influences both the thermodynamics of sea ice and the radiation field between ice and atmosphere. Spatial and temporal changes of snow fall are tremendous making its space-borne measurement a focus per se. However, the importance of snow cover for ice signatures is complex and affects both the salinity distribution and the surface roughness (Grenfell et al. 1992). Maykut and Untersteiner (1971) have estimated from field observations that the mean snow depth in the Arctic is about 0.4 m of which 0.3 m are

fallen during September and October. Ridged ice retains a thicker snow cover than level ice (Eicken et al. 1994). After onset of melt the snowcover ceases within few weeks.

While the columnar ice crystals are the predominant ice structure granular ice is another important ice constituent which can be a result of snow ice that has become saturated with water of which source may be sea water, rain water or melt water. Snow ice contains more bubbles and coarser grains than other granular ice (Tucker et al. 1992).

The temporal and spatial accumulation patterns of snow are important in controlling the sea-ice cover evolution. Excessive snow fall on ice floes can lead to sea-water flooding of the ice surface resulting in a modification of first-year or multi-year ice. Snow on new ice absorbs brine and thus substantially modifies the surface dielectric properties (Eicken et al. 1994). Average snow salinities after flooding and brine seepage show values of 4% in the Weddell Sea.

A special form of precipitation in polar areas is frost that is directly deposited at the surface by sublimation of water vapour. Depending on temperature and amount of water vapour different kinds of frost flowers can be created that have a strong impact on the radiative properties of sea ice (Drinkwater and Crocker 1988). The temporal variation of frost flowers can take place on time scales of hours. In the case of nilas formation of frost flowers is the most important process contributing to the small–scale roughness (Onstott 1992). Depending on temperature the frost flowers are composed of various crystal types like clumps, stellar dendrites and needles. Initially fresh frost flowers quickly become salty reaching salinities of 10%. Nocturnal temperature drop leads to decreased salinity of frost flowers and surface skim and additional hoarfrost accumulates on the surface. The salinity also decreases due to snow accumulation (Perovich and Richter–Menge 1994).

Frost flowers and snow on new ice substantially increase the surface roughness of the ice which is an irreversible process and therefore especially important in modifying the surface emissivity of nilas and gray ice (Onstott 1992; Lythe et al. 1993).

2.4.2 Radiative Surface–Atmosphere Interactions

Although the atmospheric impact on the remote sensing of sea ice has been acknowledged in literature (e.g. Gloersen and Cavalieri 1986) a comprehensive sea–ice–atmosphere radiative transfer model has not been described yet. So far the development of sea ice retrieval algorithms by means of radiative transport calculations is restricted to the use of effective sea ice emissivities coupled to an atmospheric RTM. The use of an effective sea ice emissivity $\varepsilon_{\nu,\zeta}$ at frequency ν and polarization ζ is based on the assumption that

only emission and reflection takes place at the surface but no transmission of atmospheric radiation into the ice and no emanation of radiation from the interior of the snow and ice bodies to the atmosphere takes place. Consequently, the surface processes are described by $\varepsilon_{\nu,\zeta}$ and a corresponding effective surface reflectivity $\varrho_{\nu,\zeta}$:

$$\varepsilon_{\nu,\zeta} + \varrho_{\nu,\zeta} = 1 \tag{19}$$

The surface-atmosphere interaction is then included in the radiative transport equation as represented for a non-scattering atmosphere in the following form:

$$\begin{aligned} L^{\uparrow}_{\nu,\zeta} = \frac{1}{2}\Big[&\varepsilon_{\nu,\zeta} B_\nu(T_S)\exp(-\delta^*_\nu/\mu) \\ &+ \int_{p_S}^{p_{Sat}} B_\nu(T)\exp(-(\delta^*_\nu - \delta_\nu(p))/\mu)d\delta_\nu(p)/\mu \\ &+(1-\varepsilon_{\nu,\zeta})\exp(-\delta^*_\nu/\mu)\int_{p_{Sat}}^{p_S} B_\nu(T)\exp(-\delta_\nu(p)/\mu)d\delta_\nu(p)/\mu \\ &+B_\nu(T_C)\exp(-\delta^*_\nu/\mu)(1-\varepsilon_{\nu,\zeta})\exp(-\delta^*_\nu/\mu)\Big] \end{aligned} \tag{20}$$

where $L^{\uparrow}_{\nu,\zeta}$ is the upwelling radiance measured by the satellite, p is the atmospheric pressure used as vertical coordinate, p_S is the surface pressure, p_{Sat} is the pressure at satellite altitude, T is temperature, T_S is the surface temperature, B is Planck's function, δ_ν is the optical depth, δ^*_ν is the total optical depth of the atmosphere, μ is the cosine of the zenith angle, and T_C is the temperature of the cosmic background. The terms on the right side of (20) represent:

- The surface emission transmitted to the satellite
- The upwelling emission of the atmosphere
- The downwelling emission of the atmosphere reflected at the surface and transmitted to the satellite
- The cosmic background radiation, transmitted to the surface, reflected at the surface and transmitted to the satellite

Various surface–atmosphere interactions for both, ocean–atmosphere and ice–atmosphere systems are handled in this way or are even more truncated (e.g. Svendsen et al. 1983; Cavalieri et al. 1984; Comiso et al. 1984; Schlüssel and Luthardt 1991; Wentz 1992; Pulliainen et al. 1993). The interaction between ice and atmosphere as defined by (19) and (20) also include a zenith angle dependency since emissivity and reflectivity depend on the incidence angle of radiation. Furthermore, this description does not allow for any interaction between snow, ice and water beneath. The emissivity, once fixed for a distinct type of sea ice has to represent a variety of compositions made of different snow and ice

types of varying thicknesses. Therefore, the approach is of limited use for the description of the radiative transfer in a coupled ice-atmosphere system.

A more complete view of the interaction between ice and atmosphere consists of an atmospheric radiation field penetrating into the ice and emission of radiation emerging from the ice into the atmosphere. Since both systems also scatter radiation the coupled interaction also contains multiple scattering processes between ice and atmosphere. The scattering processes include volume scattering in atmsophere, snow, ice and ocean as well as surface reflection at the boundaries between atmosphere and ice and between ice and ocean. Hence, the computation of the radiation field of the coupled system requires the computation of upward and downward radiances at the boundary between ice and atmosphere as well as the reflection and transmission operators of both systems. By means of a radiative transfer scheme like the MOM or SOS the multiple scattering between the two media and the transmission of radiation through the ice and atmospheric layers can be calculated as it was done by Fischer and Grassl (1984) for a coupled ocean-atmosphere system. In the case of thin sea ice and long microwaves penetrating the sea ice and the upper layers of the water body it is indicated to include the (liquid) ocean as a third medium. However, the only problem to be resolved is to successively combine two adjacent layers of which backscatter and transmission operators as well as source functions and radiances at the boundaries (or Stokes vectors in the case of polarized radiation) are known. Further layers can then be added to the combined ones. This is best illustrated by considering two layers (ice and atmosphere) represented by their boundaries (0,1) and (1,2) as shown in figure 3. The backscattering and transmission operators are specified by $\mathbf{R}_{ij}$ and $\mathbf{T}_{ij}$, respectively, where i and j represent the boundaries of a layer. The internal sources are given by the vectors $\mathbf{J}_{ij}$. The radiance vectors for upwelling and downwelling radiation, $\mathbf{L}^-$ and $\mathbf{L}^+$, respectively, are computed as follows (Plass et al. 1973):

$$\begin{aligned}
\mathbf{L}_0^- &= \mathbf{R}_{01}\mathbf{L}_0^+ + \mathbf{T}_{01}\mathbf{L}_1^+ + \mathbf{J}_{10}^+ \\
\mathbf{L}_1^+ &= \mathbf{T}_{01}\mathbf{L}_0^+ + \mathbf{R}_{10}\mathbf{L}_1^- + \mathbf{J}_{01}^+ \\
\mathbf{L}_1^- &= \mathbf{R}_{12}\mathbf{L}_1^+ + \mathbf{T}_{21}\mathbf{L}_2^- + \mathbf{J}_{21}^+ \\
\mathbf{L}_2^+ &= \mathbf{T}_{12}\mathbf{L}_1^+ + \mathbf{R}_{21}\mathbf{L}_2^- + \mathbf{J}_{12}^+
\end{aligned} \tag{21}$$

After combination of both layers the external radiance vectors should read:

$$\begin{aligned}
\mathbf{L}_0^- &= \mathbf{R}_{02}\mathbf{L}_0^+ + \mathbf{T}_{20}\mathbf{L}_2^- + \mathbf{J}_{20}^- \\
\mathbf{L}_2^+ &= \mathbf{T}_{02}\mathbf{L}_0^+ + \mathbf{R}_{20}\mathbf{L}_2^- + \mathbf{J}_{02}^+
\end{aligned} \tag{22}$$

The operators for the combined layer (0,2) or (2,0) are obtained by combination of the equations (21) to get a form like (22) and subsequent comparison of coefficients. The operators related to (0,2) and (2,0) are then given by

$$\mathbf{T}_{02} = \mathbf{T}_{12}\mathbf{X}_{02}\mathbf{T}_{01}$$

$$\begin{aligned} \mathbf{R}_{20} &= \mathbf{R}_{12} + \mathbf{T}_{12}\mathbf{X}_{02}\mathbf{R}_{r10}\mathbf{T}_{21} \\ \mathbf{J}^{+}_{02} &= \mathbf{J}^{+}_{12} + \mathbf{T}_{12}\mathbf{X}_{02}(\mathbf{J}^{+}_{01} + \mathbf{R}_{10}\mathbf{J}^{-}_{21}) \end{aligned} \tag{23}$$

and

$$\begin{aligned} \mathbf{T}_{20} &= \mathbf{T}_{10}\mathbf{X}_{20}\mathbf{T}_{21} \\ \mathbf{R}_{02} &= \mathbf{R}_{01} + \mathbf{T}_{10}\mathbf{X}_{20}\mathbf{R}_{r12}\mathbf{T}_{01} \\ \mathbf{J}^{-}_{20} &= \mathbf{J}^{-}_{10} + \mathbf{T}_{10}\mathbf{X}_{20}(\mathbf{J}^{-}_{21} + \mathbf{R}_{12}\mathbf{J}^{+}_{01}), \end{aligned} \tag{24}$$

respectively. The operators $\mathbf{X}_{02}$ and $\mathbf{X}_{20}$ describe all orders of multiple scattering between the layers (1,0) and (1,2). They can be computed according to

$$\begin{aligned} \mathbf{X}_{02} &= (\mathbf{E} - \mathbf{R}_{10}\mathbf{R}_{12})^{-1} \\ \mathbf{X}_{20} &= (\mathbf{E} - \mathbf{R}_{12}\mathbf{R}_{10})^{-1} \end{aligned} \tag{25}$$

where $\mathbf{E}$ is the unit matrix. Equations (25) represent the geometric series

$$X_{ij} = \sum_{n=1}^{\infty} (R_{1i}R_{1j})^n \tag{26}$$

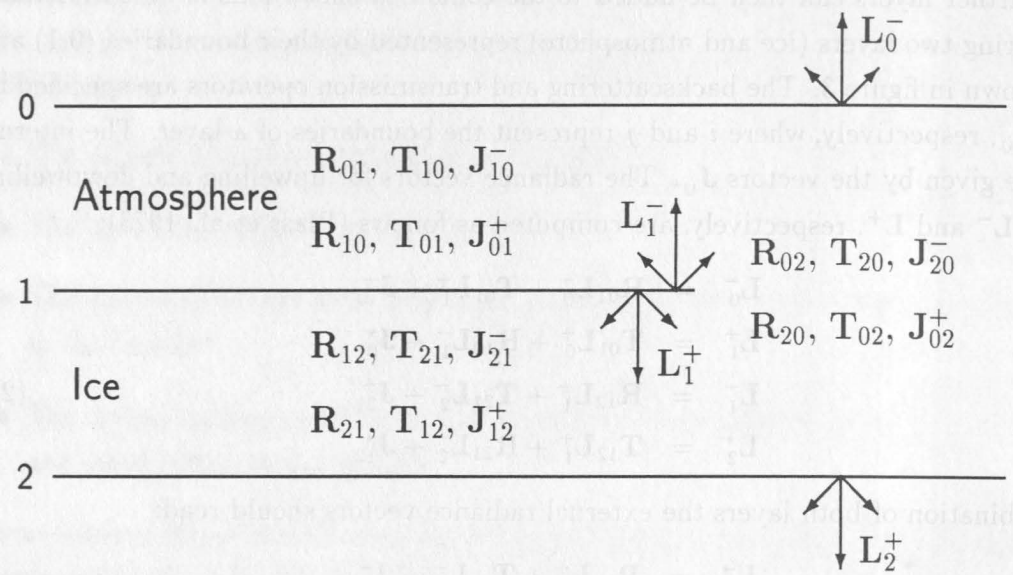

Figure 3 Schematic representation of an ice-atmosphere system and the coupling of the sublayers.

Infinitesimal surface layers describing the surface reflection can be included as described by Fischer (1983). The components of the radiance vectors $\mathbf{L}$ described above represent

radiances at different zenith angles as defined by an arbitrary Gaußian quadrature. A further expansion of the MOM for the calculation of polarized radiation is possible by replacing the radiances by Stokes vectors as shown by Bauer (1992). The backscattering and transmission operators transform into third order matrices.

2.4.3 Azimuthal Dependence

Recent research has shown that the polarized microwave radiation field shows an azimuthal dependence in cases with directional surface structures. Theoretical studies on random discrete scatterers and periodic water surfaces were performed with vector radiative transfer calculations showing that asymmetrical configurations of the scatterers can have a pronounced impact on the radiation field (Tsang 1991; Johnson et al. 1993). Especially the third component of the Stokes vector is very sensitive to the orientation distribution of scattering elements. Experimental evidence for an azimuthal dependence of the brightness temperatures at vertical and horizontal polarization over the wind–roughened ocean has been found by Wentz (1992) and Yueh et al. (1995). Anisotropic signatures of bare and snow covered sea ice have been studied theoretically by Nghiem et al. (1993) where brine inclusions in form of ellipsoidal scatterers were included in the radiative transfer simulations showing markable effects on the radiation field. Further azimuthal dependencies can be expected on a larger scale when integrating over areas covering a space–borne radiometer's field of view. In such cases one must expect anisotropic effects from leads in the pack ice. As a consequence a sophisticated coupled ice–atmosphere model should resolve the azimuthal dependence.

An azimuthally dependent radiative transfer code for the use with Stokes vectors has been described by Deuzé et al. (1989) based on the SOS method solving the problem of the radiative transfer at the highly anisotropically scattering sea surface. The Fresnel reflection matrix as well as the wave facet distribution function could be successfully developed in Fourier series. However, the inclusion of internal sources has not been realized yet. This would be a prerequisite for a coupled ice-atmosphere module at microwave frequencies.

2.5 Selection Criteria and Selection of Models

2.5.1 Sea Ice Model

From the results of the literature review it is found that various sea ice types exist in the polar regions. All these sea ice types show different radiative signatures in the microwave frequency range. Therefore the model must be highly flexible to simulate the electromagnetic properties of those sea ice types, at least for the most important ones.

In general the selection of the sea ice model must meet some requirements, which are defined as :

- simulation of the emissivity for the sea ice types on the basis of their different radiative properties in the frequency range from about 5 to 90 GHz, the limit of existing measurements allowing verification;
- allowing the specification of various ice types found in polar regions as model input;
- coupling to the atmospheric and free ocean module must be carried out by an effective quantity, which allows the combination for mixed ice conditions and free ocean, and
- results of the sea ice model have to reproduce in-situ measurements.

The development of the sea ice types mainly depends on meteorological conditions. This results in different structures on the micro and macro scale. For the micro scale the inclusion of brine pockets and air bubbles is important, because the scattering signal is influenced by these elements. Therefore the model should handle the scattering effects as discrete volume scattering especially with the consideration of the anisotropy of the brine pockets. In addition the form and concentration of the scatterers may vary with depth, as well as other parameters, e.g., salinity and ice temperature. This requires the representation of the sea ice by several layers, where the actual number required depends on the ice type. The consideration of snow covered ice is also important. Because snow acts as a dense medium the radiative effects have to be taken into account by an appropriate theory. The simulation of the radiative processes needs to include polarimetric effects. Therefore, radiative transfer models should compute the first and second Stokes parameters. However, the use of the full polarimetric theory is desirable.

From the above discussion about the radiative transfer requirements it follows that the model input specifications must allow the definition of the various parameters required to describe the ice profile including a possible snow cover.

The coupling to atmospheric module requires that the model output can be directly used as input for the atmospheric part. For the study of mixed conditions, e.g. different sea ice types or a mixture of free ocean and sea ice, the model output must allow the computation of an effective radiative quantity. This quantity must describe the radiative property of the surface for the macro-scale, e.g. satellite footprint, on the whole. An appropriate quantity which meets these requirements is the (bistatic) reflectivity matrix. The reflectivity can be transformed into the surface emissivity.

Besides the discussed requirements the reliability of the model is an equally important feature and the results of the sea ice model should fairly reproduce existing measurements.

With the above defined requirements models of type *strong fluctuation theory* are preferred. For the use in the combined model the

Many Layer Strong Fluctuation Theory Model

is recommended by the following reasons:

- sea ice profiles can be simulated by the use of distinct layers, where the number of layers is limited to computer power only;
- anisotropy effects of brine pockets can be considered by the specification of tilt and size;
- although the model is not fully polarimetric it allows to calculate both polarizations of emissivity and scattering coefficients;
- the model calculates the reflectivity matrix, which allows the direct coupling to the atmospheric and free ocean module, and
- model results show good agreement with in–situ measurements, especially at 10 GHz for horizontally polarized emissivities.

2.5.2 Free Ocean Model

The radiative signature of the free ocean surface is determined by the surface roughness and foam coverage. The surface roughness is established by waves of different types, ranging from capillary waves (small scale) to swell (large scale). The foam coverage is described by the so–called whitecaps, mainly existing on the tops of the large scale waves, and foam–streaks, which cover the ocean–surface without local preference with regard to the wave type. The development of both quantities is related to meteorological conditions, especially the wind speed. The atmospheric stability of the boundary layer also affects surface state, because it is actually determined by the friction velocity.

For the recommendation of the free ocean model the following items have to be taken into account:

- the effects of surface roughness and foam coverage should be simulated for variable meteorological conditions;
- the modeling of the surface scattering should consider the effects arising from the complete ocean–wave spectrum;

- the microwave frequency range has to be covered from about 5 to 180 GHz including polarimetry;
- coupling to the atmospheric and sea ice module has to be established through the reflectivity matrix, and
- the results of the free ocean model have to reproduce in–situ measurements.

The parameterization introduced in the literature review are based on measurements. Thus they are restricted to the meteorological conditions prevailing during the experiments. They are also confined to the electromagnetic frequency ranges, depending on the devices used for the the observations. By this the more–scale models are preferred, because they allow the simulation of the radiative signature for the required frequency spectrum with variable meteorological conditions. From the models discussed in the literature review only the three-scale model of the IfM Kiel meets the above defined requirements. The two–scale model of Guissard neglect the effects of foam and shows less than satisfactory agreements with in–situ measurements.

By these reasons the

Three-Scale Model

as established at the IfM Kiel is recommended for the combined model. It is further suggested that the foam parameterization by

Monahan and O'Muircheartaigh (1986)

is used to consider the coverage of white–caps, while the formulation of

Ross and Cardone (1974)

should be applied to consider the coverage of foam–streaks.

2.5.3 Atmospheric Model

The radiative transfer in the atmosphere is generally described by the equation of radiative transfer. Various methods for the numerical solution of this equation have been developed and are discussed in the literature review. However, the inclusion and description of radiative processes relevant for the atmosphere are most important for the selection of the model.

The recommendation for the atmospheric model thus is based on the following items:

- the treatment of radiative processes for gaseous absorption and attenuation by clouds and precipitation including polarimetry;

- specification of variable atmospheric profiles including clouds;
- coupling to the sea ice module and free ocean model has to be established by the reflectivity, and
- the results of the atmospheric model have to reproduce in–situ measurements.

The gaseous absorption of oxygen and water vapour in the atmosphere is the most important process to be simulated with the atmospheric model. From the literature review and following the suggestion of that part the gaseous absorption model by Liebe et al. (1993) is recommended. The attenuation by clouds and precipitation should be simulated by the Lorentz-Mie-theory. This is suggested, because models for non–spherical particles are still in an early stage of development. This makes them not suitable for the combined model. For the numerical solution of the radiative transfer equation the 'Discrete Ordinate Method' (DOM), 'Successive Order of Scattering' (SOS) or 'Matrix–Operator–Method' (MOM) are preferred. They show high accuracy combined with good CPU performance.

Thus for the atmospheric module the

DOM, SOS or MOM solution approach

with the use of the

gaseous absorption of Liebe (1992)

and the application of the

Lorenz-Mie-theory for the attenuation of cloud and precipitation

is suggested. It is recommended to apply the microwave model of the IfM Kiel for the combined model by the following reasons:

- the SOS method is used for the solution of the equation of radiative transfer;
- the gaseous absorption is simulated with the Liebe (1992) model;
- the application of the Lorenz-Mie-theory for the treatment of clouds and precipitation is implemented;
- arbitrary profiles of atmospheric parameter can be specified;
- coupling to the surface (ice and free ocean) is done by the reflectivity, and
- the model result shows good agreement with in situ measurements.

2.6 Atmospheric Impact on the Ice Microstructure

2.6.1 Introduction

The atmospheric impact on the ice microphysics leads to typical and discernible ice types as described in Fig. reffigweeks. On the horizontal scale of spaceborne passive microwave observations, i.e. several hundreds of km^2, the regime is dominated by mainly two ice types, first-year and multiyear ice. The occurrence of other ice types which develop mostly during the sea ice formation process is not extended enough in time and space that they would contribute significantly to sea ice signatures detected from space.

The input parameters of the sea ice module which have to be specified for each layer are given in Table 2. With six (snow) resp. seven (ice) input parameters for each layer and, say, ten layers one would easily arrive at sixty to seventy formally free parameters for each ice type. The goal of this chapter is to collect from the literature typical values for and relations between these parameters in order to diminish the effective number of free parameters. These conditions will be established from empirical observations while those resulting from known physical laws are already included in the sea ice model.

There are various investigations of microphyscal sea ice properties. Most of them refer to specific regional, seasonal or icemorphologic conditions, others present contrasting conditions. The attempt to generalize these observations may be risky in some cases, but this seems still more appropriate than ignoring them completely. If not stated otherwise, the presented parameters and relations are found in the compilation of Tucker (1992).

Table 2 Input Parameters of the Ice Module

Quantity	Symbol	Unit	Ice	Snow
Layer Depth	z	[m]	x	x
Temperature	T	[K]	x	x
Density	ρ	[g/cm^3]	x	x
Salinity	S	[‰]	x	x
Air Bubble Diameter	D_B	[mm]	x	
Brine Pocket Orientation	θ_B	[°]	x	
Brine Pocket Elogation	B_R	[1]	x	
Ice Grain Size	D_{GI}	[mm]	x	
Snow Grain Size	D_{GS}	[mm]		x
Free Water Content	l_f	[‰]		x

2.6.2 First-Year Ice

As the structure of first-year ice is mainly governed by the formation process, we will consider it in some more detail.

2.6.2.1 Formation Process

The sea ice formation starts at the water surface, induced by continued heat loss. According to the wind conditions, frazil, grease, nilas, and pancake ice may form. As these initial ice types consolidate, subsequent heat transport is hindered, and in this second phase the ice growth rate slows down. It takes place at the ice–water interface. The ice crystals grow predominantly in directions perpendicular to the crystalographic c–axis. This geometric selection process results in a columnar ice structure as depicted in Figure 4.

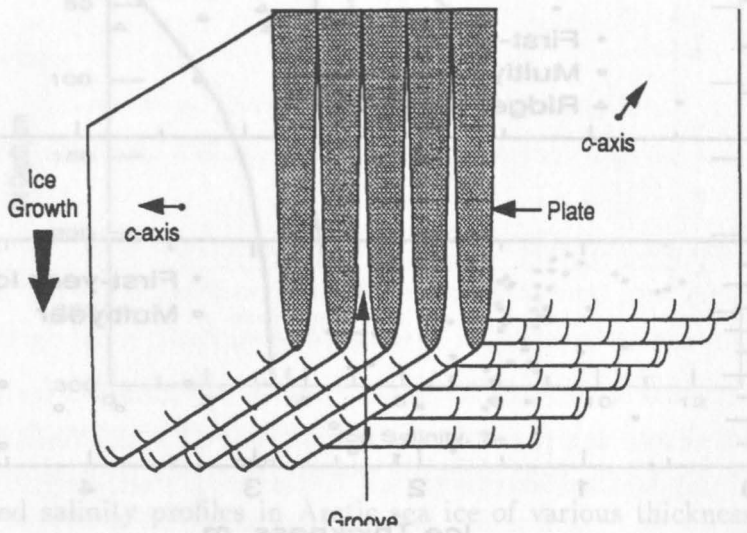

Figure 4 Dendrite and groove structure of two columnar sea ice crystals. Residual brine is trapped in groves between dendrites (plates) which remain essentially salt free. From Tucker et al. (1992) (Copyright by AGU).

Thus we find in indisturbed first–year ice three layers of texture:

- frazil layer, usually 0.05–0.1 m,
- transition layer, usually 0.05–0.1 m,
- columnar ice, remainder of the ice sheet.

While the grain size of the granular ice is typically 4–7 mm, in the columnar ice it is determined by the growth speed, i.e. fast ice growth entails small grains and vice versa. As a consequence, the grains size increases from top to bottom because the heat transport is lowered by the thicker ice sheet above during the formation process. Typical values for the grain size of columnar ice are between 5 mm at the top and 3 mm at the bottom horizontal and several decimetres vertical.

But under certain conditions granular ice may be predominant, e.g. if the ice formation at the surface prevails. This may result from an initial consolidated skim or from a freezing

snow cover after saturation with water (seawater, rainwater, meltwater). This type of ice is coarser grained and contains more air bubbles than other granular ice. The fractions of columnar and granular ice as a function of ice thickness for Arctic and Antarctic conditions are contrasted in Figure 5.

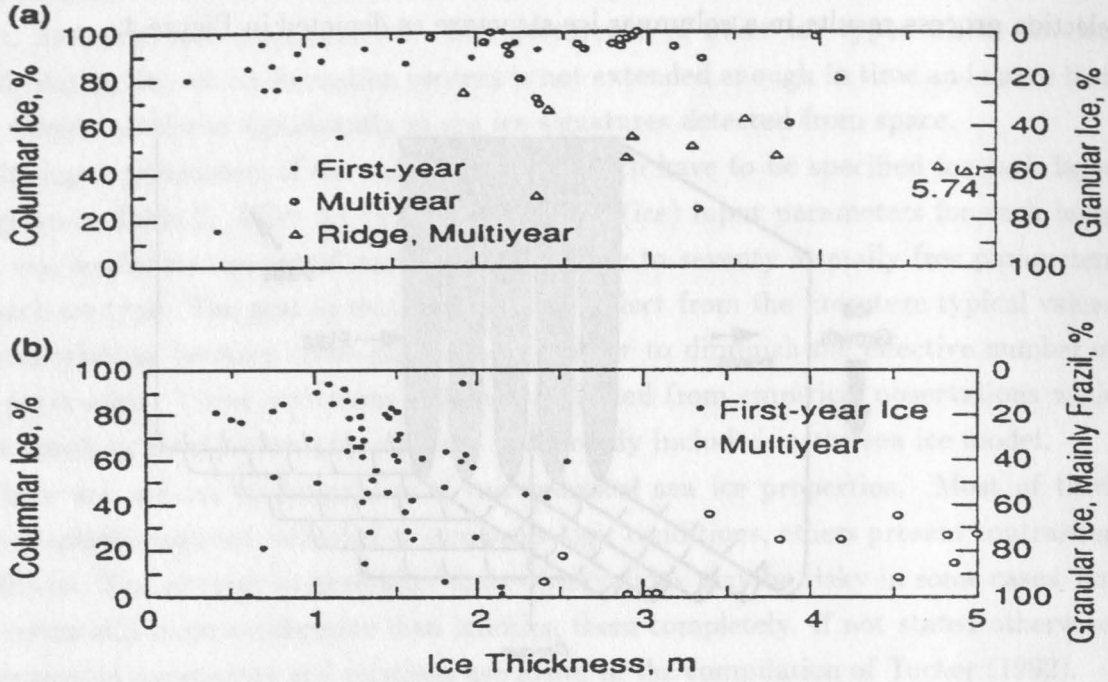

Figure 5 Percentage of columnar and granular ice versus ice thickness in floes from (a) the Fram Strait and (b) the Weddell Sea (From Tucker et al. 1992, Copyright by AGU).

While in Arctic first-year and multiyear ice the columnar ice prevails (80...100 %), its percentage is lower in Arctic ridged ice (40...60 %). In Arctic ice, there is a slight and negative correlation between percentage of columnar ice and thickness, regardless of the ice type.

2.6.2.2 Brine and Air Inclusions

As the salt is rejected almost completely from the ice crystals during the formation process, it concentrates in the brine inclusions (pockets) which are trapped in the grooves between the ice dendrites (Fig. 4). In granular ice the brine is similarly kept in the grain gaps. The fast freezing at the top causes small ice crystals with high brine inclusions, i.e. high salinity.

Once the brine is included in the ice matrix, its salinity is dictated by the conditions of phase equilibrium. Any change in temperature causes the brine pocket size to change, too. Immediately after the brine inclusion the desalination process starts, driven by gravitation and brine rejection due to temperature reduction and freezing of brine.

While these processes transport the brine downwards, in thin ice it may also be moved to the top by capillary effects and wicking up by snow and frost flowers. In total, the salinity decreases with the ice age resulting in typical C-shapes of first-year and reversed S-shapes of multiyear ice (Fig. 6).

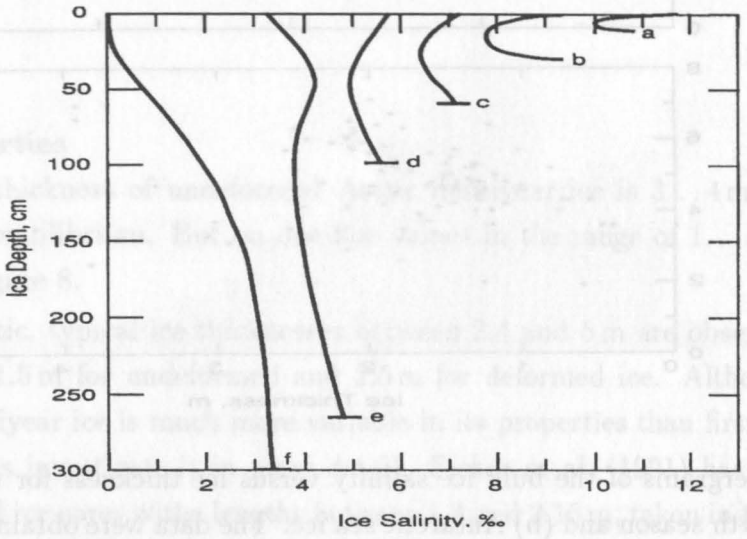

Figure 6 Idealized salinity profiles in Arctic sea ice of various thicknesses. Curves (a) through (d) represent changes observed in first-year ice. The remaining curves are for two types of profiles found in multiyear ice. Curve (e) typifies the salinity distribution beneath low areas where the surface is close to the freeboard level, while curve (f) represents the salinity profile beneath hummocks and other elevated areas (Maykut (1985), Copyright by CRC Press, Inc.)

The resulting bulk salinity of Antarctic ice relatively clearly decreases with ice thickness (Fig. 7a), while in the Arctic where multiyear ice dominates, the ice is less salty with no recognizable trend with thickness. The air volume increases with drainage from initially 0...15 ‰ up to 200 ‰ at the bottom with most frequent values in the range of 20...60 ‰. Accordingly, the density of first-year ice is typically 0.91...92 g/cm^3 with rare values between 0.89 and 0.925 g/cm^3.

Typical thicknesses of first-year ice in the Antarctic range between 0.5 and 0.75 m in the Weddell Sea and up to 3 m in coastal zones. In the Arctic on the other hand, first-year ice is only 1...2 m thick, in the Bering and Labrador Seas below 1 m. But note that the portion of first-year ice in the Arctic is much less (about 30 % of the total ice covered area) than in the Antarctic region where except in some insulated bays the complete ice coverage is newly formed every year.

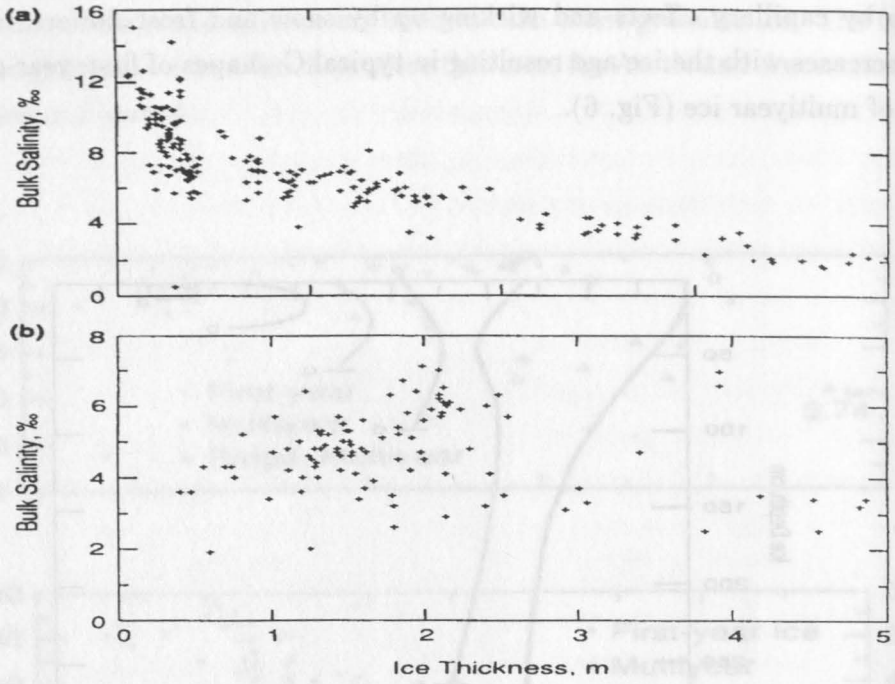

Figure 7 Scattergrams of the bulk ice salinity versus ice thickness for (a) Arctic sea ice during the growth season and (b) Antarctic sea ice. The data were obtained from a variety of published and unpublished sources (From Tucker et al. 1992, Copyright by AGU).

2.6.3 Multiyear ice

2.6.3.1 Development

The most dramatic change in the life cycle of sea ice occurs during the first melt season. The most pronounced effects is the desalination, caused by two mechanisms: First, the warming causes the ice to go into solution the brine in order to produce the new lower equilibrium salinity. As a consequence, the brine volume increases and forms larger brine pockets which join and leave channels when flowing downwards. Second, the desalination is further enhanced by flushing of the ice by surface meltwater. Both processes reduce the salt content of the upper 0.5 to 1.0 m of the sea ice from 4 to 7 ‰ before to values below 1 ‰ after the melt season. This effect leads to the lower bulk salinities in the Antarctic where multiyear ice predominates which have been shown in Figure 7. While in the Antarctic only first-year and little second-year ice occurs, the typical lifetime of Arctic ice is five to seven years. However, further melt cycles after the first one do practically not affect the ice properites, thus the notion of first-year and multi-year ice.

The recristallisation or retexturing process changes the texture during the melt cycle. Up to 1 m depth the originally sharp-edged grains become rounded, and brine pockets disappear.

Typical features of multiyear ice are melt ponds and hummocks. After the melt season,

melt ponds typically occupy 30 % of a multiyear ice surface. They are 0.5 to 1 m deep. Sometimes they melt completeley through the floe. In this case they are filled with sea water, while normally refrozen melt ponds show fresh water properties. Hummocks and pressure ridges have low salinity. About their other microphysical properties less is known, and they are investigated more in detail during the actual *Polarstern* cruise ARK XII (Eicken, private communication). Altogehter the transformation process enhances the variability of the sea ice properties considerably, as will be shown in the next section in more detail.

2.6.3.2 Properties

The typical ice thickness of undeformed Arctic multiyear ice is 3...4 m, reflecting the thermodynamic equilibrium. But on one floe values in the range of 1...12 m have been observed, see Figure 8.

In the Antarctic, typical ice thicknesses between 2.4 and 5 m are observed with most likely values at 1.5 m for undeformed and 2.5 m for deformed ice. Although it is well-known that multiyear ice is much more variable in its properties than first-year ice, only very recent works investigate it in more detail. Eicken et al. (1991) have measured the salinity of several ice cores withe lengths between 1.3 and 2.15 m, taken in the Weddell Sea in October/November 1988 and in September/October 1989, i.e. under winter conditions, see Figure 9 for sample values. The polynominal fits in Figure 10 are all rather similar with greatest variability at the top and at the bottom. The variability at the top may be explained by different fractions of granular ice, generated by recristallisation of sea ice and snow. Note the typical reversed S-shape of the salinity already shown in the idealized scetches of Figure 6. Eicken et al. (1991) conclude that the ageing process enhances the variablity.

Profiles for many input parameters have been taken during the ARCTIC91 campaign by Eicken et al. (1995). They restricted their investigation to level ice, i.e. apparently undeformed floes of at least 20 m diameter. Thus melt ponds and ridges were excluded from the investigation. The ice density increases from top to bottom (Fig. 11). For the density as well as for the salinity profiles least square fits are given (Fig. 12) which are suitable to be inserted into the sea ice module.

Profile of gas and brine volume are also given, but the ice module computes these values internally. Eicken et al. (1995) did not observe significant changes in the ice properties along the ship route which lead from older (5...7 years) to younger (1...2 years) ice. They conclude that all influences of the ice formation process are overcast during the first melt season. The variability found within one floe is as large as the one between floes of different origin or age. Thus, possible regional differences in the microwave signature of sea ice are supposed in the ice fractions not investigated here, i.e. melt ponds and pressure ridges, but the authors do not indicate the surface fractions of level ice, melt ponds and

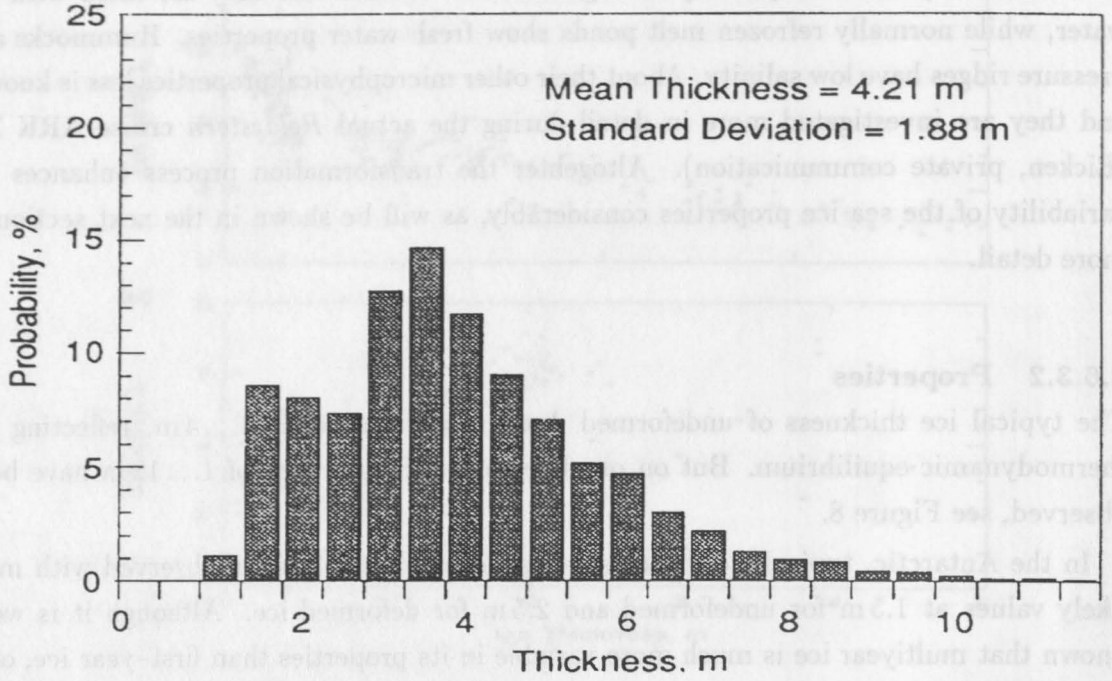

Figure 8 Probability density function of 3770 ice thickness measurements made on eight Arctic multiyear floes (From Tucker et al. 1992, Copyright by AGU).

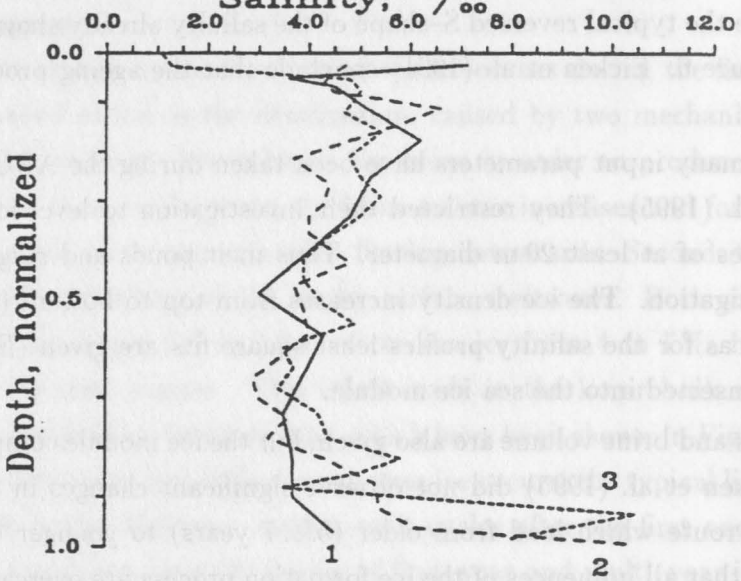

Figure 9 Salinity profiles of cores from floe 1 from Eicken et al. (1991); the curve is drawn through the midpoints of individual sections, and the depth scale is normalized to unity (Copyright by AGU).

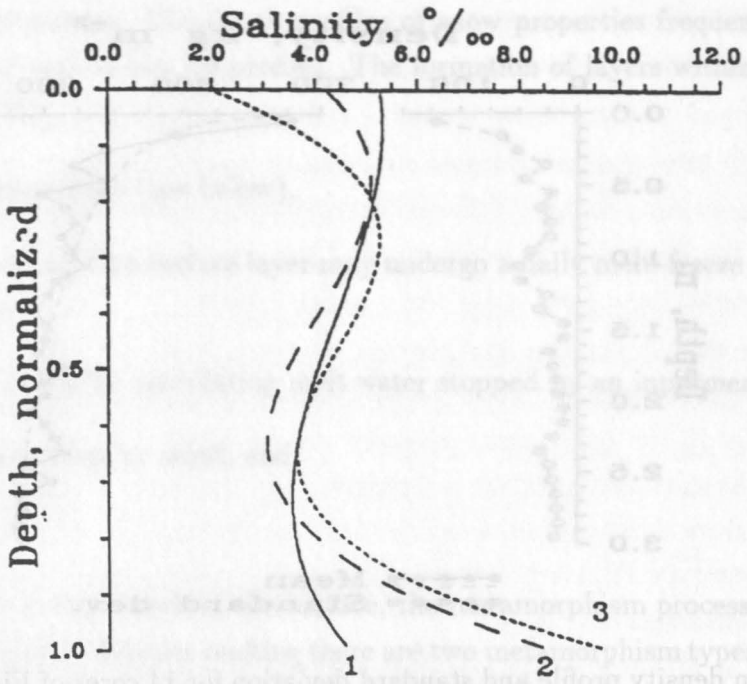

Figure 10 Polynomial fit of the salinity data shown in Fig. 9 (Eicken et al. 1991, Copyright by AGU).

ridges.

2.6.4 Snow

2.6.4.1 General Description

Snow is almost always present on top of the sea ice and influcences its microwave signature via many effects.

- It acts as a thermal insulant at the interface sea ice/atmosphere. In winter it decreases the heat exchange between ocean and atmosphere and retards freezing, while in summer the high albedo of the snow reduces the shortwave radiation thermal input delaying the melting process.
- Snow has a lower surface roughness than sea ice reducing surface scattering.
- The upper part of the salinity profile of the sea ice is influenced by diffusion and wicking up of the surface brine.
- A thick snow pack may submerge the ice floe. Flooding changes the dielectric snow properties and its salinity.

Although there are several case studies, there is no general description of how snow influences the sea ice signature.

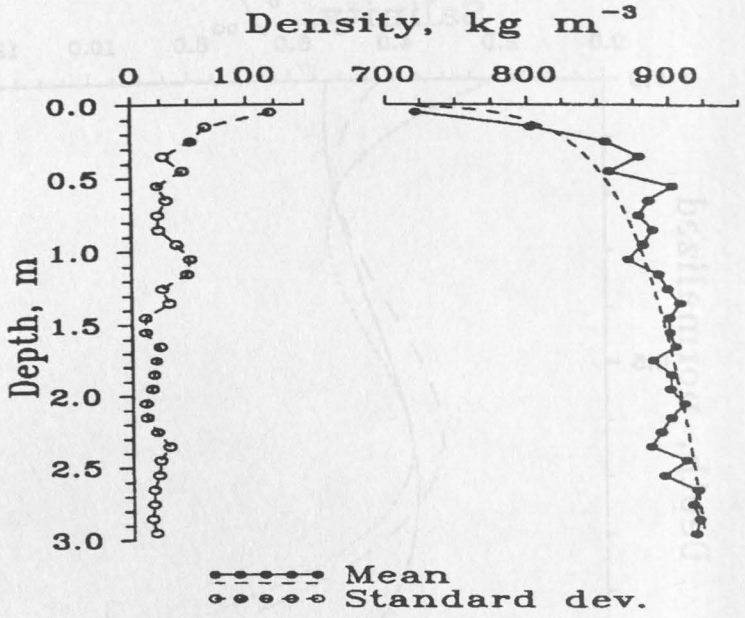

Figure 11 Mean density profile and standard deviation for 14 cores of Eicken et al. (1995). The surface layer is characterized by low densities, corresponding to large gas bubble densities. The dashed line is a least squares fit to the data of the form $\rho = 35.68 \ln(z) + 881.77$ (Copyright by AGU).

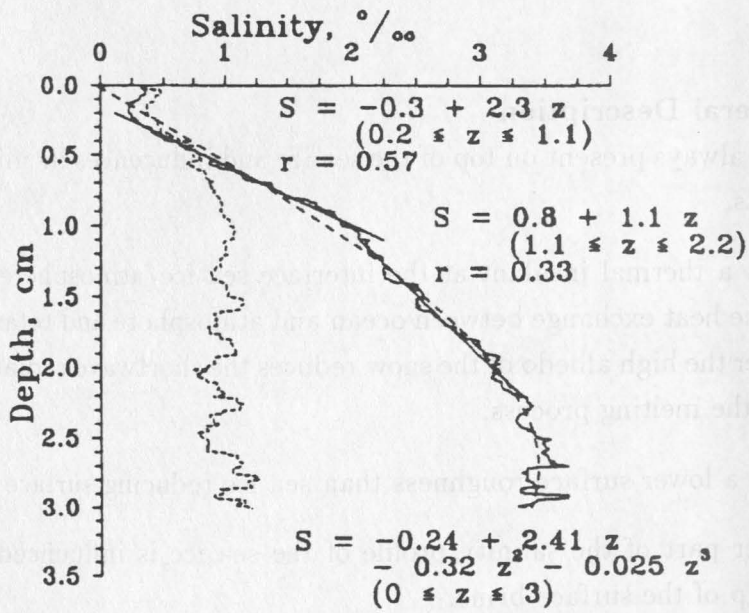

Figure 12 Mean salinity profile computed from the ARCTIC 91 cores (solid line, 0.01 m vertical resolution). Also shown are the standard deviation (dashed line at the left) and linear least square regression fits to the depth intervals 0.2–1.1 m and 1.1–2.2 m. From Eicken et al. (1995) (Copyright by AGU).

Snow shows a pronounced layering caused by the formation process and subsequent meteorological influcences. The depth profiles of snow properties frequently display discontinuities in contrast to sea ice profiles. The formation of layers within the snow pack is mainly caused by

- inner metamorphism (see below),
- solar irradiation: The surface layer may undergo a daily melt–freeze cycle producing crusted snow,
- ice lenses formed by percolating melt water stopped by an inpermeable ice layer,
- surface compacting by wind, and
- hoar.

Once the snow is deposited on the surface, the metamorphism process starts with the result of compacting it. Besides melting there are two metamorphism types. The first type is called *equitemperature* or *destructive* metamorphism. It takes place at low temperature gradients and minimizes the surface free energy. The originally dendritic crystals are transformed to more spherically shaped ones that have a minimum ratio of surface area to volume. The second type is the *constructive* or *temperature* gradient metamorphism which takes place at temperature gradients greater than 0.1 °C/cm. Water vapor diffuses from warmer to colder regions, condensates and forms new crystals. The final state, called depth hoar, consists of crystals with typical sizes in the order of millimetres. The stratification, which is not necessarily horizontal everywhere, is described by their microphysical parameters.

2.6.4.2 Quantitative Observations The most obvious snow parameter is its depth. But up to now there is no systematic investigation about the snow depth on sea ice (Tucker et al. 1992) and about the regional characteristics of snowfall. However, there have been several isolated case studies.

In the central Arctic, from August to October in the order of 0.15 m snow are deposited, until melting further 0.05 m (Untersteiner 1961) resulting in a mean snow depth of about 0.4 m, of which about 0.3 m were assumed to fall during September and October (Maykut and Untersteiner 1971). Studies in the Greenland marginal ice zone revealed that on multiyear ice much more snow is found than on first year ice. Tucker et al. 1987, observed in early summer snow depths up to 0.2 m on first–year ice with mean at 0.08 m, while on multiyear ice the snow cover ranged between 0.03 and 0.65 m with a mean at 0.28 m. Perowich et al. (1988) found in a winter experiment in the same region mean snow depths of 0.11 m on first–year and 0.47 m on multiyear ice. The snow mainly consists of wind–blown hard–packed snow of well–rounded grain with diameters ranging from 0.25 to 0.5 mm, and

the density is between 0.3 and 0.4 mg/m^3. Stratification, resulting from warm periods, is frequently found. Except for the summer melt period the snow usually remains dry.

In the Antarctic, Wadhams et al. (1987) found in the Weddell Sea quite variable snow depths with a trend to more snow at higher latitudes. Observed values ranged between 0 and 0.4 m with most typical values between 0.10 and 0.15 m. Grain sizes were found between 0.1 and 20 mm. Figure 13 shows one of the rare examples, measured by Grenfell et al. (1994) in the Weddell Sea, where most of the snow and ice profiles needed as input for the sea ice model have been measured simultaneously.

Although the snow cover acts as a thermal insulant, there is a heat transport through it, caused by three mechanisms: Heat conduction from grain to grain, vapor transport and radiation transfer in the pore space. Grenfell et al. (1989) give empirical values for the dependence of the snow/ice interface temperature as a function of surface air temperature and the temperature difference between the top and the bottom of the snow cover versus the snow thickness, see Figure 14. They also investigated the effect of the snow cover on the brightness temperature (Fig. 15).

Although the small scale roughness of frost flowers may influnce considerably the radar signature of sea ice, a variation of the passive microwave properties has not been observed (Grenfell et al. 1992).

Finally we will present two Arctic snow studies. The first one, by Barber et al. (1995) comprises all snow parameters of Table 2, but ignores the underlying sea ice. The data have been taken on landfast first-year ice in the Seasonal Sea Ice Monitoring and Modelling

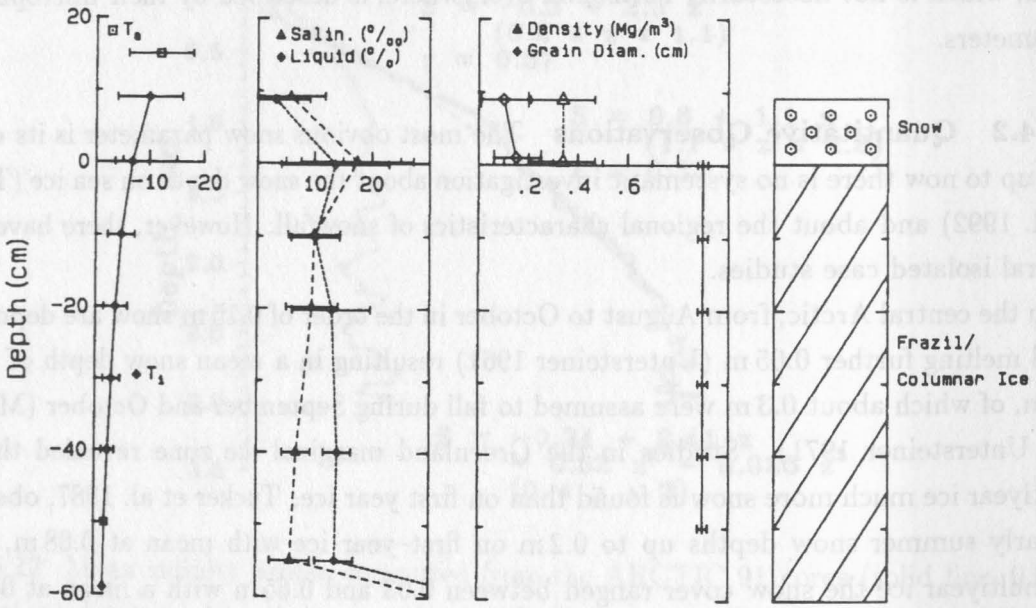

Figure 13 Mean physical properties of first-year ice at the station sites from July to November 1986 (Grenfell et al. 1994, Copyright by AGU).

Site (SIMMS) in the Resolute Bay, Northwestern Territories, Canada. The authors give for winter and melting conditions profiles of the parameterized distributions of snow grain parameters (Figs. 16 and 17), of the snow density (Figs. 18 and 19) and of the snow and sea ice salinity (Figs. 20 and 21).

The average snow temperature for cold and warm conditions (Fig. 22) clearly show distinct profiles and the snow wetness profile (Fig. 23) exhibits a considerable scatter.

Furthermore, time series of all shown parameters from mid April to mid June have been taken in order to assess the temporal development of the snow pack characteristics during the transition from freezing to melting conditions. Barber et al. (1995) conclude that under winter conditions two snow layers can be distinguished, a basal layer with large grains, more salinity and low density and a original snow layer. Under warm conditions,

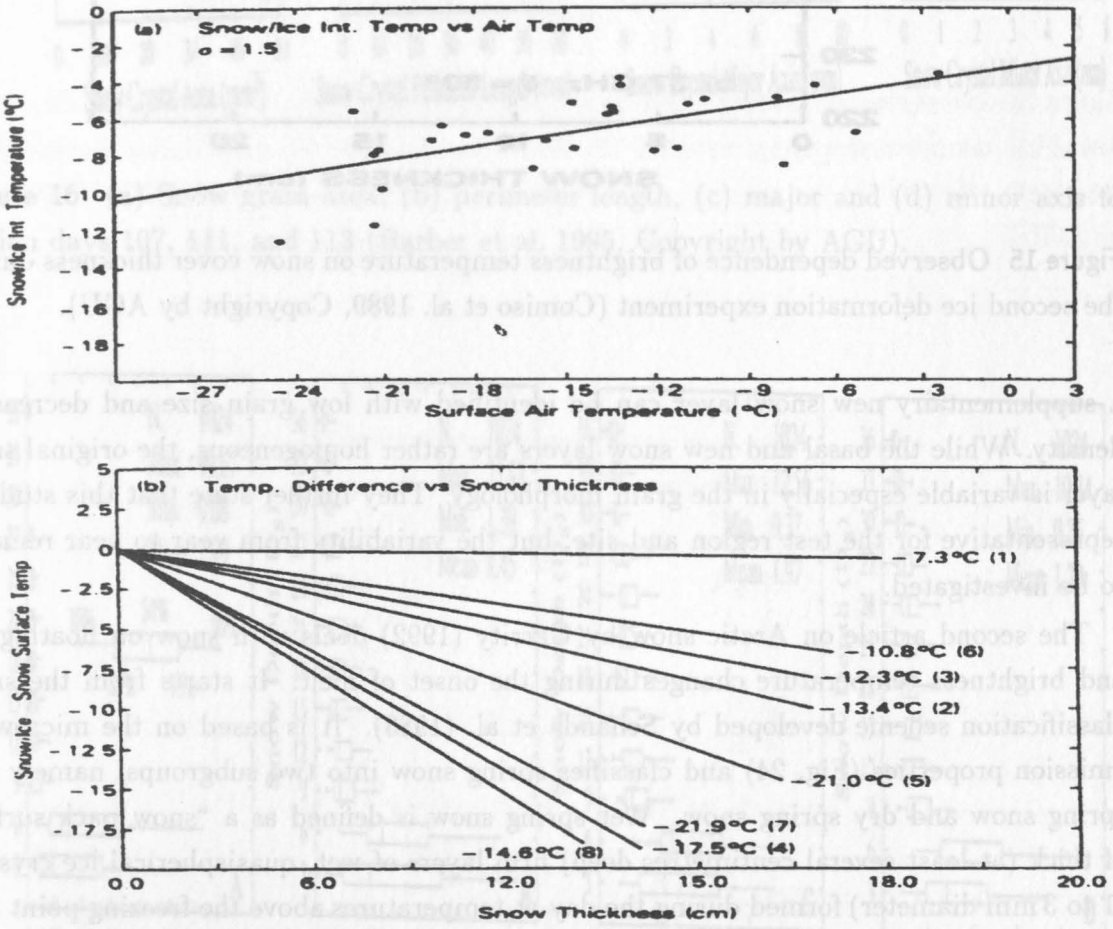

Figure 14 (a) Surface air temperature, plotted versus snow–ice interface temperatures observed during ice stations. (b) Thickness of snow cover versus the difference of snow–ice interface temperature and snow surface temperature. The different lines correspond to linear fits to measurements made during each ice station (Comiso et al. 1989, Copyright by AGU).

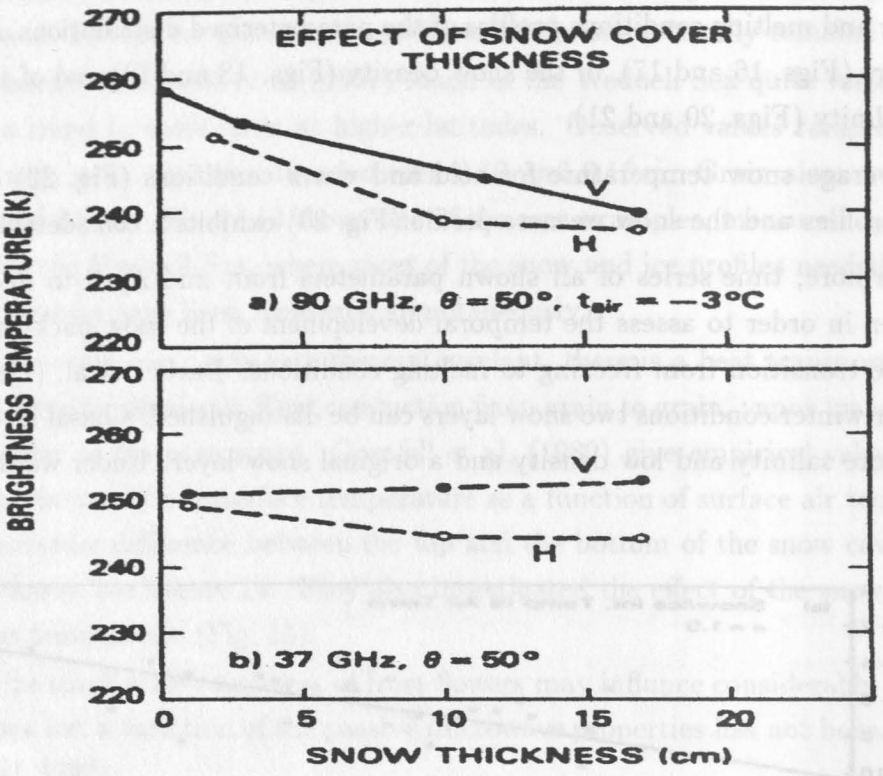

Figure 15 Observed dependence of brightness temperature on snow cover thickness during the second ice deformation experiment (Comiso et al. 1989, Copyright by AGU).

a supplementairy new snow layer can be identified with low grain size and decreasing density. While the basal and new snow layers are rather homogeneous, the original snow layer is variable especially in the grain morphology. They further state that this study is representative for the test region and site, but the variability from year to year remains to be investigated.

The second article on Arctic snow by Garrity (1992) deals with snow on floating ice and brightness temperature changes during the onset of melt. It starts from the snow classification scheme developed by Schanda et al. (1983). It is based on the microwave emission properties (Fig. 24) and classifies spring snow into two subgroups, namely wet spring snow and dry spring snow. Wet spring snow is defined as a "snow pack surface of thick (at least several centimetres deep) firm layers of wet, quasispherical ice crystals (1 to 3 mm diameter) formed during the day at temperatures above the freezing point and usually associated with either the passage of warm fronts or sunny, clear-sky conditions". Dry or refrozen spring snow has a surface snow pack "of a layer of refrozen, firm snow that forms during clear, cold nights and is several centimetres thick".

Based on this scheme, Garrity (1992) develops descriptive snow models both for Arctic (Fig. 25) and Antarctic (Fig. 26) conditions which indicate profiles of snow wetness, grain size and temperature for a variety of meteorological situations.

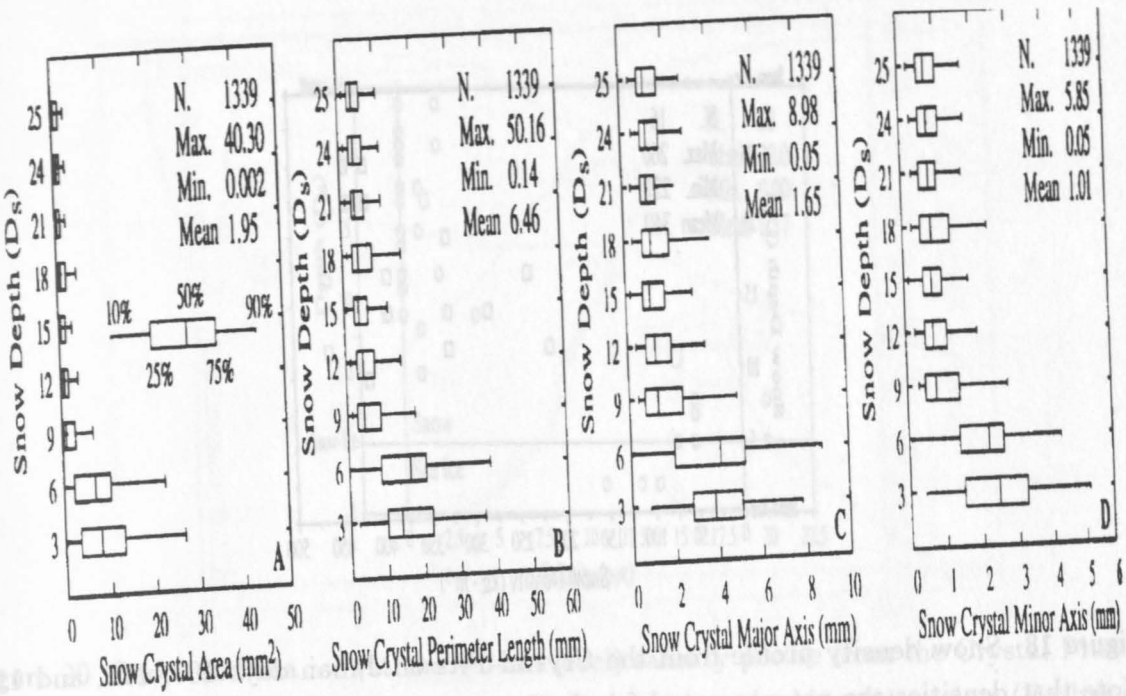

Figure 16 (a) Snow grain area, (b) perimeter length, (c) major and (d) minor axis for Julian days 107, 111, and 113 (Barber et al. 1995, Copyright by AGU).

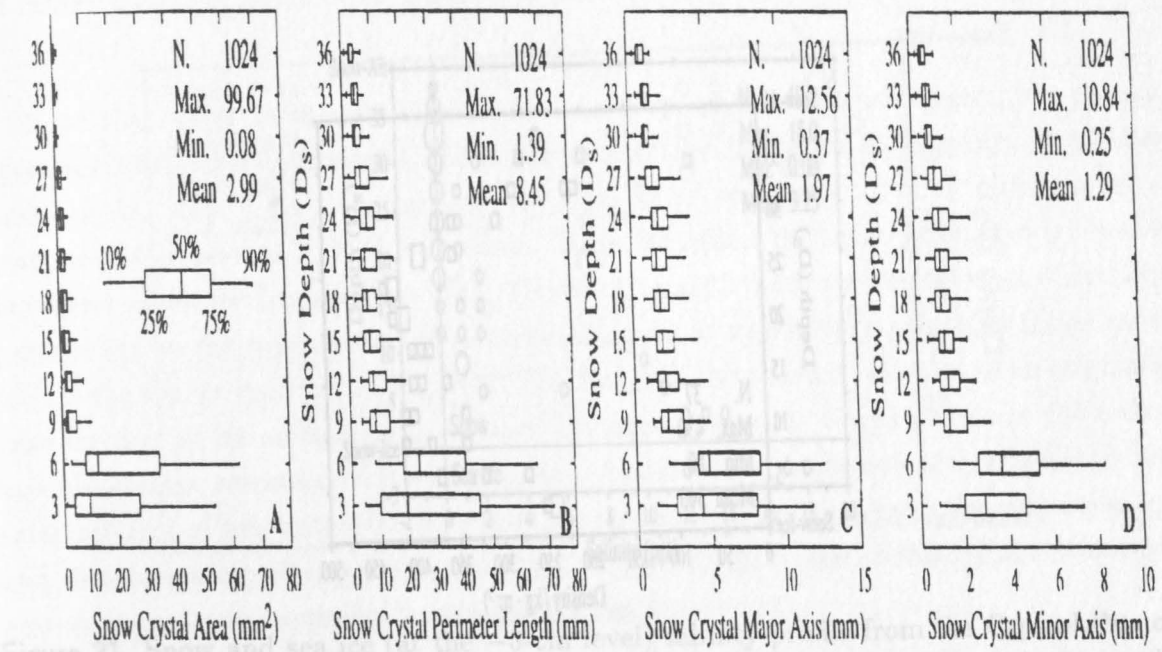

Figure 17 (a) Snow grain area, (b) perimeter length, (c) major and (d) minor axis for Julian days 164, 168, and 169 (Barber et al. 1995, Copyright by AGU).

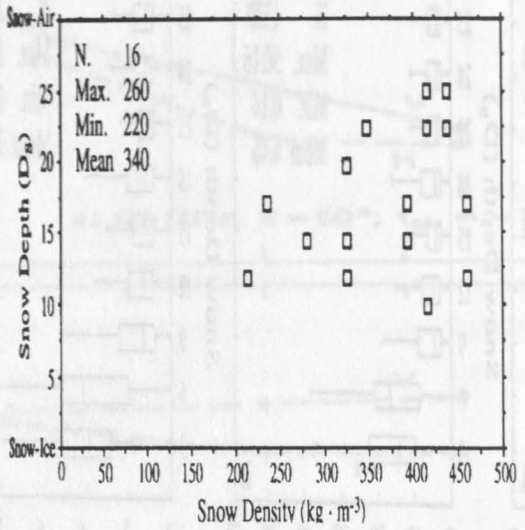

Figure 18 Snow density profile from the Crystal Pits on Julian days 107, 111, and 113. Note that densities are not presented for the 3- and 6-cm depth intervals; the snow fork data were affected by the salinity present in these layers (Barber et al. 1995, Copyright by AGU).

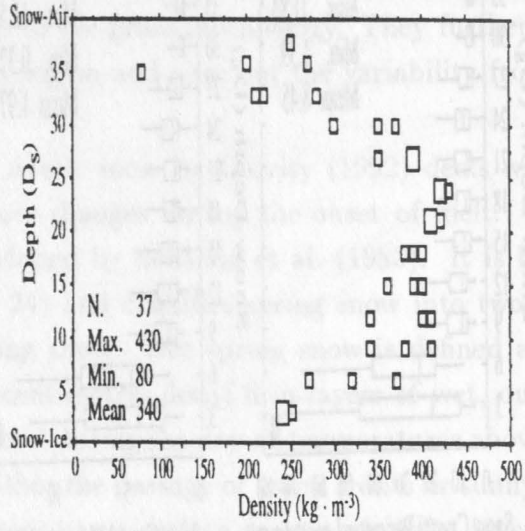

Figure 19 Snow density profile from the Crystal Pits on Julian days 164, 168, and 169. Larger symbols denote overlapping data points (Barber et al. 1995, Copyright by AGU).

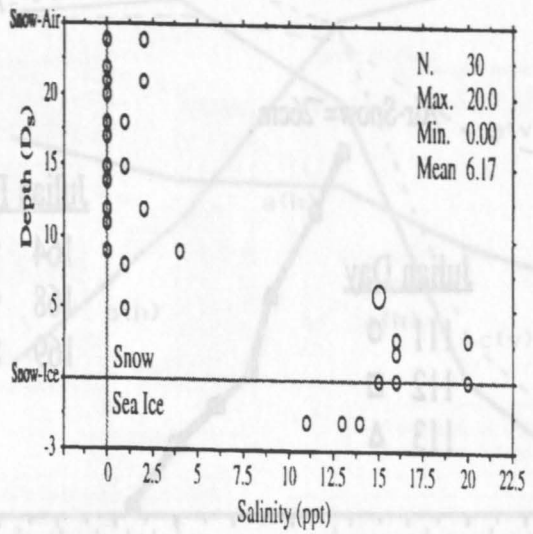

Figure 20 Snow and sea ice (at the −3-cm level) salinity profile from the Crystal Pits of Julian days 107, 111, and 113. Larger symbols denote overlapping data points (Barber et al. 1995, Copyright by AGU).

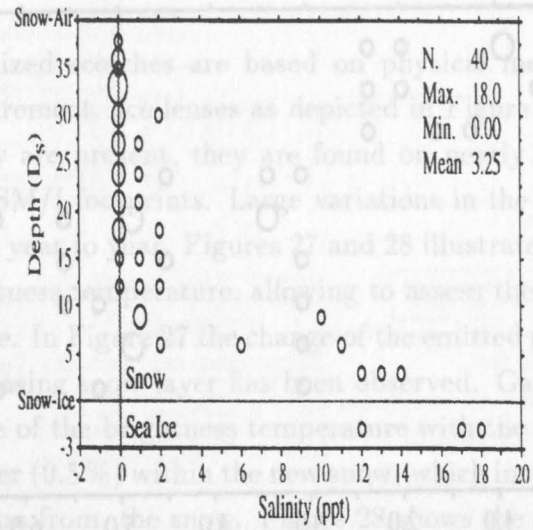

Figure 21 Snow and sea ice (at the −3-cm level) salinity profile from the Crystal Pits of Julian days 164, 168, and 169. Larger symbols denote overlapping data points (Barber et al. 1995, Copyright by AGU).